Chapter 17
Modeling the Gas Flow Process Inside Exhaust Systems: One Dimensional and Multidimensional Approaches

Gianluca Montenegro and Angelo Onorati

17.1 Introduction

Diesel engines, as a consequence of their use of lean combustion, are the main cause of on-road NO_x emissions. The most promising solution, in terms of efficiency and fuel economy, to the removal of NO_x in oxidizing condition is the use of selective catalytic reduction of NO_x (SCR) [1]. On light and heavy duty vehicles the reducing agent, namely ammonia, is obtained from a water solution of urea (commonly referenced as UWS) directly injected inside the exhaust system. The main challenge, therefore, has become the optimization of the whole process inside the exhaust system, tailoring the best removal efficiency together with a limited ammonia slip and low fuel consumption. A precise injection strategy and an efficient mixing of the ammonia with the gas stream are key factors towards the achievement of high efficiency abatements, and therefore they have become the main object of study by means of numerical simulation tools.

The modeling of SCR systems is a particularly challenging task since it involves different physical phenomena where the evolution of multiphase and multicomponent flows take place. First, a urea/water solution is sprayed into the gas stream. The dispersed multicomponent phase then evaporates and suitably mixes with the gas stream before entering the catalyst. A comprehensive understanding of the underlying flow dynamics is therefore mandatory to design an efficient $DeNO_x$ system which is characterized by a low impact on the engine performances.

From a R&D point of view, the automotive field has experienced a strong application of CFD (Computational Fluid Dynamics) tools for the design and optimization of engines and for the analysis of specific devices. Several

---

G. Montenegro (✉) · A. Onorati
Politecnico di Milano, via Lambruschini 4, Milan, MI, Italy
e-mail: gianluca.montenegro@polimi.it

A. Onorati
e-mail: angelo.onorati@polimi.it

I. Nova and E. Tronconi (eds.), *Urea-SCR Technology for deNOx After Treatment of Diesel Exhausts*, Fundamental and Applied Catalysis,
DOI: 10.1007/978-1-4899-8071-7_17,

approaches can be adopted, ranging from the 1D flow assumption to more complex multidimensional models. In particular, 1D codes have shown great flexibility of use, short calculation time, and low costs with respect to more complex multidimensional codes. Their adoption is usually motivated by the need of performing full cycle (several thermodynamic cycles) simulations of the engine coupled to the intake and exhaust system in a short time. As a matter of fact, Diesel exhaust systems are very complex, since they are always equipped with turbochargers, EGR routes, and aftertreatment devices, all of them playing an important role in the determination of the engine global efficiency. These components increase the complexity of the system and therefore the difficulty of a detailed modeling. Despite their flexibility of use and lightness, 1D models lack of predictiveness, since they cannot capture several processes occurring in the exhaust system, such as spray propagation, spray-wall interaction, and mixing processes, unless they resort to extremely simplified models of certain phenomena [2, 3]. The injection of urea/water solution, for example, can be studied in detail resorting to 3D CFD models as well as the formation of liquid film, the spray-gas mixing process, and the evaluation of ammonia distribution at the inlet of the SCR catalyst. In this chapter, it will be described the application of one-dimensional and multidimensional models for the study of the fluid dynamics of Diesel engine exhaust systems equipped with SCR systems. The 1D approach will be discussed first to highlight the importance of taking into account the overall engine configuration and the aspects of flow unsteadiness. Multidimensional approaches are usually focused on smaller details, such as the fluid dynamic analysis of the mixer and its interaction with the injected spray, rather than on the whole engine.

17.2 1D Models for the Prediction of Gas Flows

In the last decades, 1D models have been widely used for multiple purpose in the field of internal combustion engines and several codes are available on the market and in academies, both for commercial and research purposes [4–6]. Historically, different discretization approaches have been followed, but the most common are based on finite difference and finite volume ones, confining the finite element method only to research applications [7]. The finite volume and finite difference approaches are based on the formulation of 1D conservation equation of mass, momentum, and energy for an unsteady and reacting flow. Usually, the level of simplification reached in a 1D model allows to neglect the viscosity of the fluid and to lump the viscous phenomena into a gas-wall friction coefficient [8].

Applying the balance of mass, momentum, and energy to a generic control volume identified by a portion of a pipe with variable cross-section (Fig. 17.1), the conservation equations can be written in the following way:

$$\frac{\partial(\rho F)}{\partial t}+\frac{\partial(\rho u F)}{\partial x}=0, \qquad (17.1)$$

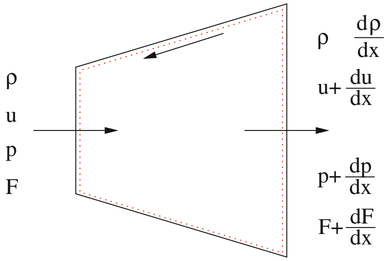

Fig. 17.1 Control volume used to derive the 1D conservation equations

$$\frac{\partial(\rho u F)}{\partial t}+\frac{\partial(\rho u^2 F+pF)}{\partial x}=p\frac{\partial F}{\partial x}x-\frac{2}{D}\rho u|u|f_{\mathrm{w}}F, \tag{17.2}$$

$$\frac{\partial(\rho e_0 F)}{\partial t}+\frac{\partial(\rho e_0 u F+upF)}{\partial x}=\rho q_{\mathrm{re}}F. \tag{17.3}$$

The governing equations can then be written in vectorial form as follows:

$$\frac{\partial \mathbf{W}(x,t)}{\partial t}+\frac{\partial \mathbf{F}(\mathbf{W})}{\partial x}+\mathbf{B}(\mathbf{W})+\mathbf{C}(\mathbf{W})=0 \tag{17.4}$$

$$\mathbf{W}(x,t)=\begin{bmatrix}\rho F\\ \rho u F\\ \rho e_0 F\\ \rho \mathbf{Y} F\end{bmatrix},\quad \mathbf{W}(\mathbf{F})=\begin{bmatrix}\rho u F\\ pF+\rho u^2 F\\ \rho u h_0 F\\ \rho \mathbf{Y} F\end{bmatrix},\quad \mathbf{B}(\mathbf{W})=\begin{bmatrix}0\\ -p\frac{dF}{dx}\\ 0\\ 0\end{bmatrix},$$
$$\mathbf{C}(\mathbf{W})=\begin{bmatrix}0\\ \rho G F\\ -\rho(q+q_{\mathrm{re}}+q_{ev})F\\ -\rho\dot{\mathbf{Y}}F\end{bmatrix}, \tag{17.5}$$

where **W** is the vector of the conserved variables, **F** is the vector of the fluxes of the conserved variables and vector **B** takes into account the effect of the cross-section variation. Vector **C** accounts for the contributions of: (i) the heat exchanged between the gas and the pipes (q); (ii) the heat generated by the homogeneous reactions occurring in the exhaust line (q_{re}); and (iii) the friction between the gas and the walls (G). The system of equations is then closed by the state equation of the gas, which is treated as a mixture of perfect gases whose specific heat capacity is a function of both chemical composition and temperature [9]. The composition of the gas can then be tracked solving the conservation equation for each chemical component present in the gas phase. The vector Y in Eq. (17.5) refers to the mass fraction of each species composing the gas and allows to transport along the ducts all the information related to the chemical composition of the mixture. In these models, an arbitrary number of chemical species can be considered, depending on the particular chemical process that one wants to simulate. In any case, the gas composition can be assigned as a boundary condition, if the modeling is focused only onto a single device of the exhaust system, or eventually assigned by a specific combustion model in the case the simulation involves the complete engine configuration (intake system, cylinders, and exhaust system). For the modeling of exhaust systems of Diesel engines a typical gas composition that can be taken into account may be O_2, N_2, Ar, CO_2, H_2, CO, NO, C_xH_y, NH_3, HNCO (isocyanic acid), NH_2–CO–NH_2 (urea) plus two phases of water, $H_2O_{(l)}$, and $H_2O_{(g)}$:

$$\mathbf{Y} = \begin{bmatrix} Y_1 \\ Y_2 \\ \vdots \\ Y_{N_S} \end{bmatrix} \sum_{j=1}^{N_S} Y_j = 1. \tag{17.6}$$

The source term $\dot{\mathbf{Y}}$ in **C** (Eq. 17.5) expresses the production/destruction rate of the *j*th specie during the transport, due to reactions in the exhaust manifold (gas-phase reactions) and in the chemical converters (solid phase reactions). In the set of conservation equations, water appears into two phases, gaseous and liquid. The liquid phase can be considered as a property advected with the gas, in the same way the gaseous species are transported. This assumption can only be accepted if the size of the liquid water droplets is very small, which is rarely the case when urea–water solution is injected in the gas stream.

The system of Eq. (17.4) is a partial derivative hyperbolic system, whose numerical solution is achieved using shock-capturing numerical methods [10–13]. These methods are characterized by second-order accuracy and therefore they give rise to spurious oscillation when high gradients are present in the solution field. To suppress the occurrence of numerical instabilities, flux limiting techniques, or gradient limiters are used [8].

17.2.1 Modeling the Thermal Aspects

An accurate prediction of the chemical behavior of aftertreatment devices, can be achieved throughout a correct prediction of the heat fluxes along the exhaust system. This aspect is also important for a correct prediction of the back pressure which, in the end, affects the volumetric efficiency of the engine determining an increase of fuel consumption. In particular, to simulate engine driving cycles with cold start, in which the thermal transient of the exhaust system affects the performance of the catalytic converters, the correct estimation of the heat loss is vital. Also from a point of view of optimization, the estimation of the heat loss becomes important, especially in those cases where the improvement of the manifold insulation is tailored, in order to achieve an higher gas temperature at the inlet of the catalytic devices [3, 14]. The prediction of the thermal transient of the exhaust system can be carried out by considering the heat transferred between the gas and the walls in the energy balance of the gas, as a source term in Eq. (17.6), and solving a coupled Fourier equation applied to the pipe walls, whose thermal balance can be expressed by:

$$\begin{aligned}\int\limits_{V_{\mathrm{w}}} \rho_{\mathrm{w}} c_{\mathrm{p,w}} \frac{\partial T_{\mathrm{w}}}{\partial t} = & \int\limits_{V_{\mathrm{w}}} \operatorname{div}(\lambda \operatorname{grad} T) \mathrm{d}V \\ & + \int\limits_{V_{\mathrm{w}}} S_{\mathrm{e,c}} \, \mathrm{d}V.\end{aligned} \tag{17.7}$$

Since the heat flux given by the temperature gradient between the wall and the gas bulk has been imposed as a boundary condition, Eq. (17.7) can be reduced to the following expression:

$$T_{\mathrm{w}}^{\mathrm{n}+1} = T_{\mathrm{w}}^{\mathrm{n}} + \frac{\Delta t}{\rho_{\mathrm{w}} c_{\mathrm{p,w}} V_{\mathrm{w}}} \left(Q_{\mathrm{r}} + Q_{\mathrm{h}} + Q_{\lambda}^{\mathrm{ax}} + Q_{\lambda}^{\mathrm{r}} + S_{\mathrm{e,c}} \right), \tag{17.8}$$

where T_{w}^{n+1} and T_{w}^{n} are, respectively, the wall temperatures at the new and old time step, while Q_{r} is the heat flux due to radiative heat transfer, Q_{h} is the convective heat flux between the gas and the walls, $Q_{\lambda}^{\mathrm{ax}}$ and Q_{λ}^{r} are, respectively, the conductive heat in the axial direction inside the wall and in the radial direction, when layers of different materials are considered. The source term $\mathrm{S}_{\mathrm{e,c}}$ accounts for the heat released by eventual chemical reactions or condensation and evaporation processes occurring in the proximity of the pipe walls. The quantities $\mathrm{c}_{\mathrm{p,w}}$, ρ_{w}, and V_{w} are, respectively, the wall specific heat capacity, the wall density and the volume of material related to the single computational cell. The Fourier equation can be applied to each layer of material, in order to consider the effects of different material properties on the global heat flux with the surrounding air (e.g., insulating materials, metallic shells, air gaps, or wash-coat layers). Several correlations can be used to model the heat transfer between the gas and the walls, however, the most general correlation appears to be the one proposed by Churchill, since its range of validity for the Reynolds and Prandtl number are those typical of the flow regimes inside exhaust systems of internal combustion engines [14, 15]:

$$\mathrm{Nu} = \sqrt[10]{\mathrm{Nu}_{\mathrm{l}}^{10} + \left(\frac{e^{(2200-\mathrm{Re})/365}}{\mathrm{Nu}_{\mathrm{l}}^{2}} + \frac{1}{\mathrm{Nu}_{\mathrm{t}}^{2}} \right)^{-5}}, \tag{17.9}$$

where

$$\mathrm{Nu}_{t} = \mathrm{Nu}_{0} + \frac{0.079 (f/2)^{\frac{1}{2}} \mathrm{Re} \mathrm{Pr}^{\frac{5}{6}}}{1 + \mathrm{Pr}^{\frac{4}{5}}}, \tag{17.10}$$

$$\mathrm{Nu}_{0} = 4.8, \tag{17.11}$$

$$\mathrm{Nu}_{l} = \begin{cases} 2.97 & \text{square flow section,} \\ 3.675 & \text{circular flow section,} \\ 3.0 & \text{triangular flow section.} \end{cases} \tag{17.12}$$

This correlation is valid for $0 < \mathrm{Pr} < 10$ and for $0 < \mathrm{Re} < 10^6$, therefore, considering that inside I.C. engine exhaust systems the Prandtl number is usually lower than 1 and Re is that typical of fully turbulent flow regimes, this correlation can be applied to the study of exhaust gas flows. The friction coefficient f that appears in Eq. (17.10) is given by the Churchill correlation as well [16]:

$$f = 2\left[\left(\frac{8}{\mathrm{Re}}\right)^{12} + \frac{1}{(A+B)^{\frac{3}{2}}}\right]^{\frac{1}{12}}, \tag{17.13}$$

where

$$A = \left[2.2088 + 2.457\ln\left(\frac{\varepsilon}{d} + \frac{42.683}{\mathrm{Re}^{0.9}}\right)\right]^{16}, \tag{17.14}$$

$$B = \left(\frac{37.530}{\mathrm{Re}}\right)^{16}. \tag{17.15}$$

The same correlation for the friction coefficient is also used to define the source term of the momentum conservation (Eq. 17.2).

17.2.1.1 Effect of Moisture Condensation and Evaporation

The prediction of the thermal transient of the exhaust systems, especially in the case of cold start, can be further improved by modeling the formation of a liquid film layer due to the condensation, and its subsequent evaporation, of the water vapor contained in the exhaust gas (usually around 7–8 % of mass fraction). From the analysis of the temperature history gauged by thermocouples along the exhaust system, it has been pointed out the presence of a plateaux due to the insulation effect produced by the evaporation of the liquid film layer [17–19]. This effect is negligible in the hot part of the exhaust line close to the engine head, but becomes important in the low temperature part and in particular inside of catalysts and Diesel particulate filter substrates, due to the high specific surface per unit volume. To predict the effect of the moisture condensation and evaporation, it is necessary to consider the mass transfer of water to the walls during the condensation and the migration of water vapor from the walls to the exhaust gas during the evaporation. Condensation is the cause for the increase of the wall temperature during the first seconds of operating conditions, while the evaporation becomes responsible of an insulation effect due to the latent heat of evaporation taken from the gas. The latent heats of evaporation and condensation ($\Delta h_{\mathrm{e,c}}$) in the model can be taken into account in the source term $\mathrm{S}_{\mathrm{e,c}}$ of the Fourier equation (Eq. 17.8). The rate of phase change (evaporation or condensation) $\dot{Y}$ in Eq. (17.6) can be expressed by the following equation [17]:

$$\dot{Y}_{\mathrm{H_2O}} = \rho k_{\mathrm{m,H_2O}} S \left(\frac{1}{\rho v_{\mathrm{sat}}} - C_{\mathrm{s,H_2O}} \right), \tag{17.16}$$

in which the specific volume of the saturated water vapor v_{sat} has been determined as a function of the wall temperature on the basis of tabulated values:

$$v_{\mathrm{sat}} = e^{1.325 \cdot 10^{-4} T_{\mathrm{w}}^2 - 0.06 T_{\mathrm{w}} + 5.175}. \tag{17.17}$$

The above expression is valid only for 20 °C < T_{w} < 120 °C. In the temperature range considered for the evaluation of the saturated water vapor's specific volume, a constant value of 2,370.1 kJ/kg can be assumed for the latent heat with good accuracy. The source term for the thermal balance of the pipe walls is therefore:

$$S_{\mathrm{e,c}} = \dot{Y}_{\mathrm{H_2O}} \Delta h_{\mathrm{e,c}}. \tag{17.18}$$

17.2.1.2 Water Dragging Model

The water mass in direct contact with the gas stream inside the pipe is dragged in the direction of the flow by the friction between the water surface and the gas. The theory of multiphase flow is very complex and far from the complexity degree of a 1D model. The two phase flow inside the monolith can therefore be reduced to a stratified layer flow, where the two phases are moving with different velocities. The reasons of the water motion can be: (i) motion caused by the friction between the gas and the water and (ii) effect of the gravity if the pipe is not horizontal. The mass of dragged liquid is determined by applying the mass and momentum conservation to the two phases, the liquid water and the exhaust gas, calculating the contact surface on the basis of the water layer thickness [20, 21]. Referring to Fig. 17.2 and assuming that the two phases are confined in the two regions A_{l} and A_{g}, respectively, for liquid and gas, the velocity of the liquid can be calculated by the following equation:

$$\frac{\tau_{\mathrm{l}} S_{\mathrm{l}}}{A_{\mathrm{l}}} - \frac{\tau_{\mathrm{g}} S_{\mathrm{g}}}{A_{\mathrm{g}}} - \tau_{\mathrm{i}} S_{\mathrm{i}} \left(\frac{1}{A_{\mathrm{l}}} + \frac{1}{A_{\mathrm{g}}} \right) + \left(\rho_{\mathrm{l}} - \rho_{\mathrm{g}} \right) g \sin \beta = 0, \tag{17.19}$$

where

$$\begin{aligned} \tau_{\mathrm{l}} &= \frac{1}{2} f_{\mathrm{l}} \rho_{\mathrm{l}} |v_{\mathrm{l}}| v_{\mathrm{l}}, \\ \tau_{\mathrm{g}} &= \frac{1}{2} f_{\mathrm{g}} \rho_{\mathrm{g}} |v_{\mathrm{g}}| v_{\mathrm{g}}, \\ \tau_{\mathrm{i}} &= \frac{1}{2} f_{\mathrm{i}} \rho_{\mathrm{g}} |v_{\mathrm{g}} - v_{\mathrm{l}}| \left(v_{\mathrm{g}} - v_{\mathrm{l}} \right). \end{aligned} \tag{17.20}$$

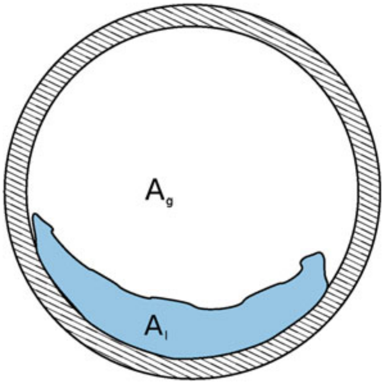

Fig. 17.2 Example of the distribution of the two phases in a channel section

The terms $\mathbf{f}_l$, $\mathbf{f}_{g,\ i}$ are, respectively, the friction terms for the liquid-wall, gas-wall, and gas–liquid interface, while β is the inclination angle of the pipe with respect to an horizontal line. Once the liquid velocity v_l has been calculated, the new value of the liquid mass in each calculation node can be determined resorting to an upwind finite difference calculation technique.

17.2.1.3 Urea–Water Solution Injection

Another important aspect that can be considered in 1D models is the injection of water urea solution. The approach must be very simple but at the same time should be able to account for the main effects of the injection of liquid droplets. As anticipated in Sect. 17.2.1.2, the conservation equations for each chemical species may account for the liquid phase of water. The assumption is arguable, since droplets exchange momentum with the gas stream and they have also inertia. However, to model the impact of liquid droplets on the gas-phase heat balance and the release of urea, it may be acceptable.

Once injected, the number of droplets is fixed and advected with the gas stream. The injected spray does not exchange, for simplicity sake, momentum with the exhaust gas; however, since the temperature gradient between the droplet and the gas is high, the droplet undergoes a heating process until it reaches the saturation temperature. This phase can be divided into two steps (summarized in Fig. 17.3):

- the droplet is heated until the saturation temperature is reached,
- the water contained in the droplet evaporates until its mass fraction becomes null. In this process, the evaporation rate depends on the heat made available by the gas stream.

During the heat up phase the energy balance of the droplet states that its energy variation is given by the heat transferred to the droplet by convection:

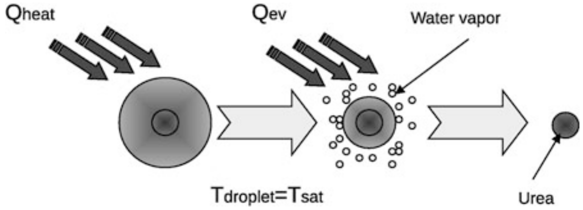

Fig. 17.3 Schematic of the heat up and evaporation process of a water urea solution droplet modeled in 1D

$$\frac{4}{3}\pi R_\mathrm{p}^3\rho_\mathrm{p}c_\mathrm{pr}\frac{\mathrm{d}T_\mathrm{p}}{\mathrm{d}t} = \left(4\pi R_\mathrm{p}^2\right)k\frac{T_\mathrm{g}-T_\mathrm{p}}{2r_\mathrm{p}}\mathrm{Nu_I}, \tag{17.21}$$

where R_p, T_p, ρ_p e c_pr are respectively the diameter, the temperature, the density, and the specific heat of the droplet. T_g is the gas temperature and k is the thermal conductivity of the gas. The heat exchanged between the gas and the droplet can be expressed as:

$$q = h_\mathrm{p}A_\mathrm{s,p}\left(T_\mathrm{g}-T_\mathrm{p}\right), \tag{17.22}$$

where h_p is the convective heat exchange coefficient given by the following relation:

$$h_\mathrm{p} = \frac{k\mathrm{Nu_I}}{2r_\mathrm{p}}, \tag{17.23}$$

and $A_\mathrm{s,p}$ is the surface of the droplet:

$$A_\mathrm{s,p} = 4\pi R_\mathrm{p}^2. \tag{17.24}$$

The Nusselt number $\mathrm{Nu_I}$ in Eq. (17.23) is described by the following relation [22, 23]:

$$\mathrm{Nu_I} = 2.0 + 0.6\,\mathrm{Re}^{\frac{1}{2}}\,\mathrm{Pr}^{\frac{1}{3}}, \tag{17.25}$$

where the Reynolds number, Re, is referred to the droplet velocity and diameter. Properties of viscosity, specific heat capacity, and conductivity are evaluated as functions of the average temperature defined as follows:

$$\widehat{T} = \frac{T_\mathrm{g}+2T_\mathrm{p}}{3}, \tag{17.26}$$

Solving the energy balance of the droplet (Eq. 17.21) with respect to the droplet temperature, the following equation can be obtained:

$$\frac{\mathrm{d}T_\mathrm{p}}{\mathrm{d}t} = \frac{3}{2}\frac{k\mathrm{Nu_I}}{R_\mathrm{p}^2\rho_\mathrm{p}c_\mathrm{pr}}\left(T_\mathrm{g}-T_\mathrm{p}\right). \tag{17.27}$$

This approach is supported by the assumption that the number of injected droplets does not change and that the mean droplet diameter is also transported as a property along the gas stream. When water is up to the saturation temperature, the evaporation process is dominant and the whole heat exchanged between the gas and the droplets is used to evaporate the liquid. The rate of evaporation is therefore proportional to the energy made available by the gas through convection:

$$\dot{m}_{H_2O} = \frac{\rho_{vp} c_{pr} D_{H_2O} \frac{T_g - T_p}{2R_p} \mathrm{Nu}_{II}}{\Delta h_{fg}} A_{s,p}, \tag{17.28}$$

where ρ_{vp} is the density of the liquid vapor, D_{H_2O} is the diffusion coefficient of gaseous water in air, Δh_{fg} is the latent heat of evaporation. The Nusselt coefficient Nu_{II} is defined in a different way, with respect to the Nu_I, since it accounts for reduction of the evaporation rate due to the presence of a vapor layer over the droplet surface:

$$\mathrm{Nu}_{II} = \left(2.0 + 0.6\,\mathrm{Re}^{\frac{1}{2}}\,\mathrm{Pr}^{\frac{1}{3}}\right) \frac{\ln\left(1 + B_p\right)}{B_p}, \tag{17.29}$$

where B_p is the Spalding transfer number [24], which is driven by the gradient of concentration between the saturated vapor and the gas stream.

17.2.2 Thermal and Hydrolytic Decomposition of Urea

In mobile applications, the SCR technique involves the atomization of aqueous solution of urea in the hot part of the exhaust system upstream the SCR catalyst. The urea injected undergoes two different chemical processes to produce the ammonia necessary to sustain the SCR reaction: thermal decomposition and hydrolysis.

17.2.2.1 Thermal Decomposition of Urea

When a solution of urea is injected into the exhaust system, the first process that takes place is the evaporation of the water contained in each droplet. After the water evaporation, the urea is thermolyzed by the surrounding hot gas, producing gaseous ammonia and isocyanic acid according to the following reaction:

$$NH_2 - CO - NH_{2(s)} \rightarrow NH_{3(g)} + HNCO_{(g)}. \tag{17.30}$$

This mechanism, however, can be considered as a single-step reaction only if the heating is carried out fast. A slow heating of the urea will produce side reactions, due to the high reactivity of isocyanic acid, with the production of undesirable chemical products such as biuret, triuret, and cyanuric acid [25]. Usually, the reaction is supposed to occur without any side effect and is endothermic (+185.5 kJ at standard conditions).

17.2.2.2 Hydrolysis of Isocyanic Acid

The step following the thermal decomposition of urea is the catalyzed hydrolysis of the isocyanic acid formed in the previous reaction. The isocyanic acid is hydrolyzed by the water contained in the gas stream according to the following reaction:

$$HNCO_{(g)} + H_2O_{(g)} \rightarrow NH_{3(g)} + CO_{2(g)}. \tag{17.31}$$

This reaction completes the process of urea decomposition, transforming the isocyanic acid into further ammonia delivered to the SCR reactor. The reaction enthalpy of hydrolysis indicates that the reaction is exothermic, bringing a heat generation of 95.9 kJ per mole. This aspect is important, since it can be a consistent contribution to the heat request of reaction 17.30, reducing to less than half the heat required by the thermal decomposition. The global process, therefore, can be seen as the reaction:

$$NH_2 - CO - NH_{2(s)} + H_2O_{(g)} \rightarrow 2NH_{3(g)} + CO_{2(g)}, \tag{17.32}$$

in which the heat required is 89.6 kJ per mole.

17.2.3 Kinetic Model

The chemical reactions can be modeled by means of the source term $\dot{\mathbf{Y}}$ of Eq. (17.6), which expresses the rate of change of the transported chemical species:

$$\dot{\mathbf{Y}} = \begin{bmatrix} \dot{Y_1} \\ \dot{Y_2} \\ \vdots \\ \dot{Y_{N_S}} \end{bmatrix} \propto \begin{bmatrix} \frac{dc_1}{dt} \\ \frac{dc_2}{dt} \\ \vdots \\ \frac{dc_{N_S}}{dt} \end{bmatrix}. \tag{17.33}$$

The model for the urea decomposition considers the following reactions:

$$NH_2 - CO - NH_{2(s)} \rightarrow NH_{3(g)} + HNCO_{(g)}, \tag{17.34}$$

$$HNCO_{(g)} + H_2O_{(g)} \rightarrow NH_{3(g)} + CO_{2(g)}. \tag{17.35}$$

The rate of reaction (17.34) can be considered as first order with respect to the concentration of urea [26]:

$$r_1 = -k_1 C_{CO(NH_2)_2}. \tag{17.36}$$

The same consideration applies to the calculation of the reaction rate of Eq. (17.35), which is assumed to be a function of the concentration of water and isocyanic acid:

$$r_2 = k_2 C_{\mathrm{HNCO}} C_{\mathrm{H_2O}}. \tag{17.37}$$

The rate of change of the species taken into account by the model is therefore given by the following equations:

$$\frac{\mathrm{d}C_{\mathrm{CO(NH_2)_2}}}{\mathrm{d}t} = -k_1 C_{\mathrm{CO(NH_2)_2}}, \tag{17.38}$$

$$\frac{\mathrm{d}C_{\mathrm{HNCO}}}{\mathrm{d}t} = k_1 C_{\mathrm{CO(NH_2)_2}} - k_2 C_{\mathrm{HNCO}} C_{\mathrm{H_2O}}. \tag{17.39}$$

The reaction scheme presented above, according to experimental measurements available in the literature [26], is characterized by different values of the kinetic constants k_i, depending whether they occur onto a catalyzed bed or not. Focusing on the urea thermal decomposition process, experiments [26] have shown that reaction (17.38) is very rapid and is not affected by the presence of a catalyzed bed of typical SCR systems, whereas the hydrolysis of isocyanic acid occurs only at high temperature levels. According to this analysis, the values of the kinetic constants that can be used for the simulation of urea thermal decomposition are:

$$k_1 = 4.9 \times 10^3 e^{\frac{-5505}{\mathrm{RT}}}, \tag{17.40}$$

$$k_2 = 2.5 \times 10^5 e^{\frac{-14861}{\mathrm{RT}}}, \tag{17.41}$$

An example of the application of a 1D model for the simulation of thermal decomposition of urea can be found in Montenegro and Onorati [2]. Usually, the solver is optimized just for the gas dynamics and not for the stability of the reaction mechanism. As a matter of fact, the reaction mechanisms may be quite stiff and therefore require very small time steps. The problem can be overcome adopting a smaller time step also for the CFD, however this strategy may be not convenient when several seconds of real time need to be simulated. Hence, stable ordinary differential equation (ODE) solvers [22] are adopted in order to handle the reaction mechanism. In particular, given a time step Δt_{CFD} for the gas dynamics, whose choice for explicit methods is ruled by the CFL criterion [27], the integration of the chemistry is performed following subcycles of integration to solve the ODE system per each gas dynamic time step:

$$\frac{\mathrm{d}Y_{\mathrm{i}}}{\mathrm{d}t} = \dot{Y}_{\mathrm{i}} = \omega_{\mathrm{i}}, \tag{17.42}$$

where ω_i expresses the rate of change, due to heterogeneous reactions, of the *i*th chemical component:

$$\omega_{\mathrm{i}} = \frac{Y_{\mathrm{i}}^{\mathrm{t}+\Delta\mathrm{t}} - Y_{\mathrm{i}}^{\mathrm{t}}}{\Delta t}. \tag{17.43}$$

It has been demonstrated that the measurements of Yim could be reproduced numerically with fairly good agreement using the kinetic constants determined experimentally on the test rig [2].

In Figs. 17.4 and 17.5, it is shown a comparison between the measured and calculated gas composition downstream of a thermal reactor as a function of temperature at two different space velocities, namely 32,000 and 65,000 h^{-1}. The feeding gas has been assigned with a fixed composition according to the measurements in [26]: 250 ppm of urea, 5 % O_2, 2 % H_2O, and 93 % N_2. Due to thermal decomposition, the quantity of ammonia at the reactor outlet increases with the catalyst temperature. The reaction scheme included in the 1D model has shown a good reliability, since it is capable of predicting the composition trend at the thermal reactor outlet at different gas temperature levels. Moreover, the influence of the space velocity variation can be captured correctly. The presented model can, therefore, be applied to a 1D model of an engine coupled to the intake and exhaust systems. The liquid phase injected in the system can be tracked as a scalar quantity representing the amount of water injected during a time step. Assuming a typical number of droplets on the basis of modeling experience in the field of liquid sprays, it is possible to estimate the amount of evaporated water and urea by means of heat transfer correlations. The advantage of this approach is that the unsteadiness of the process is fully captured, allowing to account for contributions such as temperature discontinuities and heat losses on the thermal decomposition of urea. An example of application on a real engine geometry, comprehensive of the chemistry occurring also in the catalysts, can highlight the importance of a whole engine simulation. The test case considered is an heavy duty 4.0 L four cylinder diesel engine running at full load at 1,000 rpm. Figure 17.6 shows a 1D schematic of that engine where three different reacting regions have been highlighted, namely the thermolizer, the hydrolyzer, and the SCR catalyst.

The results presented in Fig. 17.7 show the concentration profile of the main chemical species considered, along a typical Diesel engine exhaust system, in which the three reacting regions have been supposed at a fixed temperature of 523 K. In particular, it can be noticed the abatement of the nitrogen oxide only inside the SCR reactor, with the consequent decrease of ammonia. This conversion efficiency is low because of the lack of NH_3, that is completely exploited in this reactor. The ammonia, as can be seen, is produced mainly by the thermal decomposition of urea. In this operating condition the engine presents no ammonia slip at the tailpipe outlet, but a non-negligible quantity of isocyanic acid and urea would be discharged in the atmosphere. These results point out that a 1D computational model can be a useful tool to optimize the urea injection strategy, in order to reduce both the NO_x emission and the slip of dangerous substances like HNCO and ammonia. On balance, the 1D approximation has the main limit of needing the definition of several tuning factors, such as friction factors, heat exchange coefficients, and so on. These aspects are mainly related to the assumption of uniform distribution of thermal and fluid dynamic quantities. A correct prediction of the heat flux between the gas and the external ambient can be assessed only with an accurate resolution of the near-wall temperature gradient, as well as the flow resistance needs to be estimated resolving the near-wall velocity gradient. All these aspects are modeled in 1D codes resorting to empirical correlation. If we consider SCR systems, flow resistance and heat losses are not the

Fig. 17.4 Comparison between calculated and measured HNCO, urea, and NH_3 concentration at the outlet of the thermolysis reactor as a function of the gas temperature with a space velocity of 65,000 h^{-1}

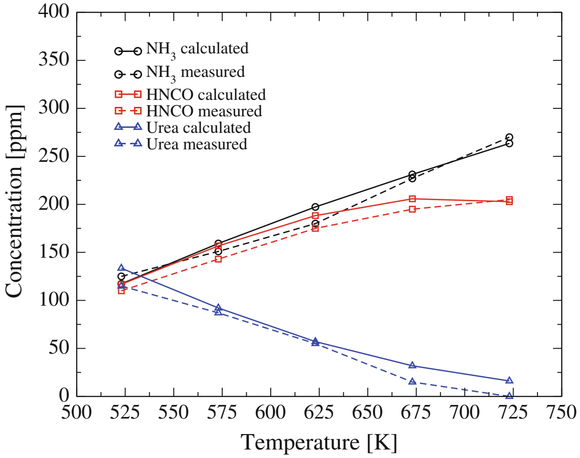

Fig. 17.5 Comparison between calculated and measured HNCO, urea, and NH_3 concentration at the outlet of the thermolysis reactor as a function of the gas temperature with a space velocity of 32,000 h^{-1}

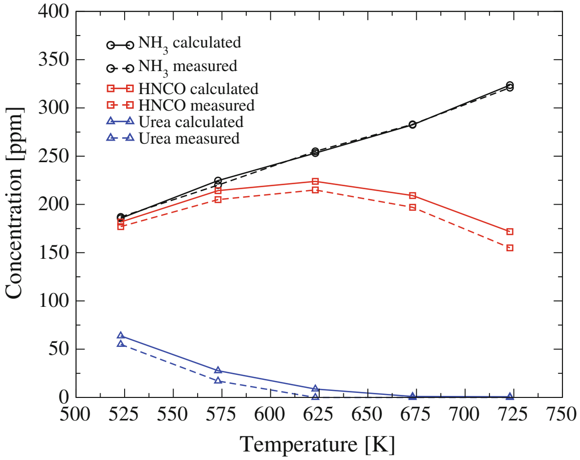

only aspects that matter during the design phase. As a matter of fact, the injection of UWS sprays requires usually the adoption of a mixing device, whose main role is to provide a distribution of reducing agent as much uniform as possible over the catalyst inlet section. This requirement is demanded by the one to one molar ratio between nitrogen oxides and ammonia of the standard SCR reaction. Since the NO_x is uniformly distributed along the surface, its abatement is ensured by an equivalent distribution of ammonia. The lower is the uniformity of the reducing agent, the lower will be the catalyst efficiency. A 1D model is not able to capture the distribution on the flow area of a chemical specie and the mixing process of the reducing agent with the gas stream cannot be determined, unless further tuning parameters are introduced. For this reasons a finer optimization of an SCR system

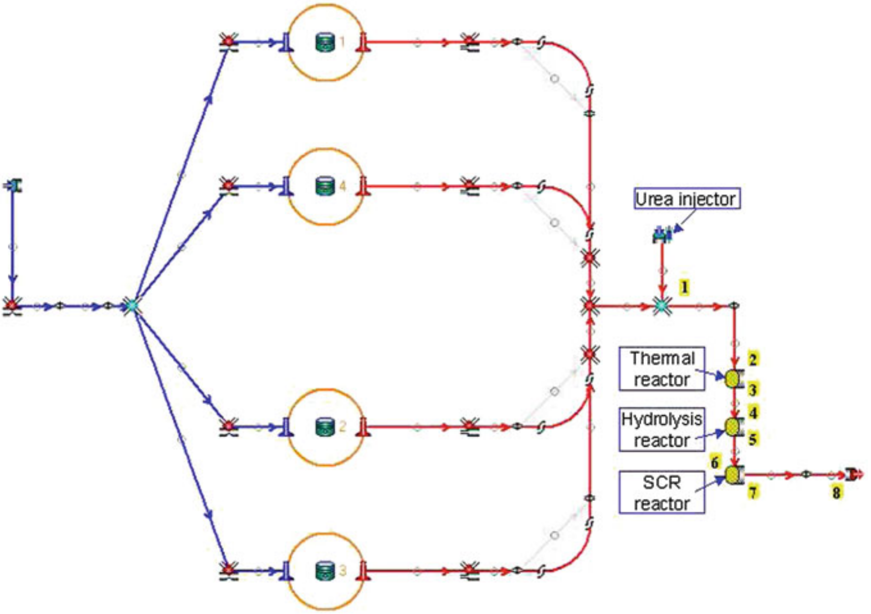

Fig. 17.6 Schematic of the 4.0 L heavy duty Diesel engine used for the simulation of the complete SCR system under unsteady flow condition

cannot be performed resorting exclusively to a 1D analysis, but requires the aid of a deeper investigation of specific aspects, such as the gas-spray interaction and mixing, which can only be carried out resorting to multidimensional codes.

17.3 Multidimensional Models

17.3.1 Governing Equations

When gradients and field non uniformities along the flow section become guiding factors of specific phenomena, such as gas mixing and spray evolution, the modeling of these effects is regarded as fundamental to perform an accurate prediction. In this scenario, the adoption 3D CFD codes represents the only feasible way to follow. Among all the models available, the most used are based on the finite volume approach for the discretization of partial derivative equations. This formulation allows to express the set of equations in a conservative way for any arbitrary mesh shape, without limiting the choice of the grid typology to be used. Defining an arbitrary control volume, the integration of the conservation equation can be generally expressed in the following form:

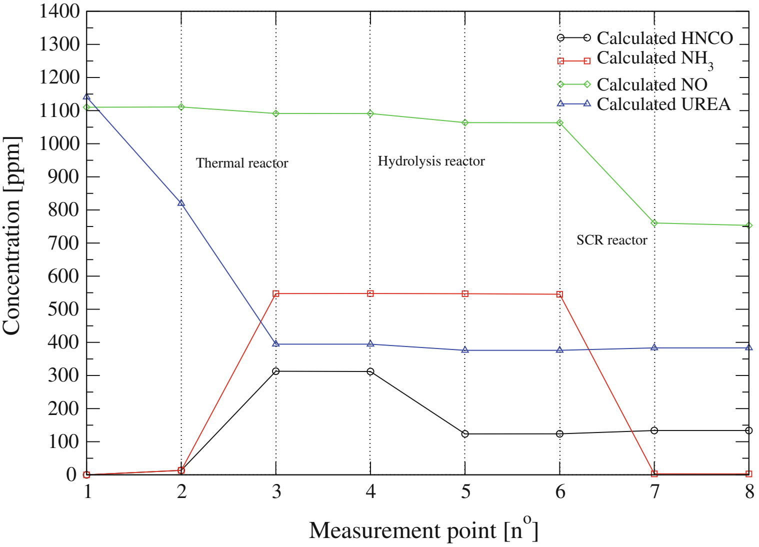

Fig. 17.7 NH_3, HNCO, urea, and NO concentrations tracked along the exhaust system with reactors at 523 K

$$\int_V \frac{\partial(\rho\phi)}{\partial t}\mathrm{d}V + \int_S \rho\phi\mathbf{U}\cdot\mathbf{n}\mathrm{d}S = \int_S Q_S(\phi)\cdot\mathrm{n}\mathrm{d}S \int_V Q_V(\phi)\mathrm{d}V \tag{17.44}$$

where the variable ϕ represents a generic conserved variable and $\mathbf{Q}_\mathrm{S}$ and Q_V are surface and volume source terms, respectively. Performing the integral operation and assuming ϕ as the gas density ρ, Eq. (17.44) leads to the multidimensional conservation equation of mass:

$$\frac{\partial\rho}{\partial t} + \nabla\cdot(\rho\mathbf{U}) = \dot{\Omega}. \tag{17.45}$$

This represents the overall mass conservation without referring to the chemical composition of the gas. The source term of Eq. (17.45) takes into account the mass exchange between the liquid and the gas phase. Since the liquid phase can be present into two different forms, droplets coming from the injection of the water solution and liquid film deposited onto the walls, two distinct terms have been included in this equation:

$$\dot{\Omega} = \dot{\Omega}^{\mathrm{Spray}} + \dot{\Omega}^{\mathrm{WallFilm}}. \tag{17.46}$$

The exhaust gas of an internal combustion engine is usually composed by multiple chemical components (O_2, CO_2, NO_x, and other compounds) each of them is advected along the gas stream. Despite no diffusion of mass is considered in Eq. (17.45), a single component may diffuse due to gradients in the composition.

In particular, gradients in chemical composition are present at interfaces between liquid and gas and also inside the gas, whenever the concentration of a single component changes. These are typically originated by the opening of the exhaust valve at the end of each combustion process. For this reason, additional equations are solved for every chemical component:

$$\frac{\partial}{\partial t}(\rho Y_{\mathrm{i}})+\nabla\cdot(\rho\mathbf{U}Y_{\mathrm{i}})=-\nabla\cdot(\rho\Gamma_{\mathrm{k}}\nabla Y_{\mathrm{k}})+\dot{\Omega}_{\mathrm{k}}^{\mathrm{Chemistry}}+\dot{\Omega}_{\mathrm{k}}^{\mathrm{Spray}}+\dot{\Omega}_{\mathrm{k}}^{\mathrm{WallFilm}}. \tag{17.47}$$

This equation accounts for the presence of convection, diffusion, and source terms due to the occurrence of chemical reactions and to the presence of an evaporating wall film and liquid spray. The mass diffusion coefficient Γ is determined assuming the Fick's law of binary diffusion of a single component into a multicomponent mixture. The momentum equation can be derived from Eq. (17.44) assuming that the quantity ϕ represents a vectorial quantity $\mathbf{U}$:

$$\frac{\partial}{\partial t}(\rho\mathbf{U})+\nabla\cdot(\rho\mathbf{U}\mathbf{U})=-\nabla p+\nabla\cdot\tau+\rho\mathbf{f}+\xi. \tag{17.48}$$

The term τ is the viscous stress tensor and can be expressed in a complete form as:

$$\tau=\mu\left[\nabla\mathbf{U}+(\nabla\mathbf{U})^{T}\right]-\frac{2}{3}\mu\nabla\mathbf{U}\cdot\mathbf{I}. \tag{17.49}$$

The other two terms $\mathbf{f}$ and ξ account for body forces, such as gravity, and the momentum exchange between the gas and the liquid spray, respectively.

The last conservation equation that can be formulated to completely define the thermo-fluid dynamic state of a fluid is the conservation equation of energy. The total internal energy is a quantity that well represents the thermodynamic state of the fluid:

$$E=U(p,T,\omega_{\mathrm{k}})+E_{\mathrm{k}}=U+\frac{1}{2}\mathbf{U}\cdot\mathbf{U}, \tag{17.50}$$

With regard to energy conservation equation, we must consider the two types of fluxes, namely the convective and the diffusive (thermal conductivity of the fluid):

$$\mathbf{F}_{\mathrm{C}}=\rho E\mathbf{U},\quad \mathbf{F}_{\mathrm{D}}=-k\nabla T. \tag{17.51}$$

The volume source terms are the work of the volume forces f_{e} plus the heat sources (radiation, reactions or electrical resistance) given by:

$$Q_{\mathrm{V}}=\rho\mathbf{f}_{\mathrm{e}}\cdot\mathbf{U}+q_{\mathrm{H}}. \tag{17.52}$$

The surface sources $\mathbf{Q}_{\mathrm{S}}$ are the result of the work done on the fluid by the internal shear stress acting on the surface of the control volume:

$$\mathbf{Q}_{\mathrm{S}}=\sigma\cdot\mathbf{U}=-p\mathbf{U}+\tau\cdot\mathbf{U}. \tag{17.53}$$

Considering all this contributions, the final formulation of the energy conservation equation becomes the following:

$$\frac{\partial \rho E}{\partial t} + \nabla \cdot (\rho E \mathbf{U}) = \nabla \cdot (k \nabla T) + \nabla \cdot (\sigma \cdot \mathbf{U}) + \rho \mathbf{f}_{\mathrm{e}} \cdot \mathbf{U} + q_{\mathrm{H}}. \tag{17.54}$$

17.3.1.1 Modeling the Turbulence

The Navier–Stokes equations do not require assumptions about the particular type of flow taken into account; however, a comprehensive simulation of a turbulent flow would require a space and time discretization capable of resolving the Kolmogorov microscale and the time characteristic associated with it [28]. This approach is extremely onerous from the computational point of view, since the microscale scales with the inverse of $\mathrm{Re}^{\frac{3}{4}}$ [29, 30]. The direct solution of the Navier–Stokes equations is therefore not the suitable approach for the majority of the problems encountered in practice. For this reason, a modeling of the turbulent phenomena is needed to achieve accurate results and to reduce the computational cost of simulations. In practice, the quantities can be expressed as a mean value, plus a fluctuation due to randomness of the process considered. By performing a suitable averaging process, the Reynolds averaged Navier–Stokes (RANS) equations can be obtained, in which the average of the fluctuating component gives rise to additional term in Eqs. (17.47), (17.49), and (17.54):

$$\frac{\partial \rho}{\partial t} + \nabla \cdot (\rho \mathbf{U}) = \dot{\Omega}^{\mathrm{Spray}} + \dot{\Omega}^{\mathrm{WallFilm}}, \tag{17.55}$$

$$\frac{\partial}{\partial t}(\rho \mathbf{u}) + \nabla \cdot (\rho \mathbf{U}\mathbf{U}) = -\nabla p + \nabla \cdot \tau' + \rho \mathbf{f} + \xi, \tag{17.56}$$

$$\frac{\partial \rho E}{\partial t} + \nabla \cdot (\rho E \mathbf{U}) = \nabla \cdot (k \nabla T) + \nabla \cdot (\tau' \cdot \mathbf{U}) + \rho \mathbf{f}_{\mathrm{e}} \cdot \mathbf{U} + q_{\mathrm{H}}, \tag{17.57}$$

where

$$\tau' = \tau(\mu) + \tau_{\mathrm{turb}}(\mu_{\mathrm{t}}), \tag{17.58}$$

$$k' = k(\mu) + k_{\mathrm{turb}}(\mu_{\mathrm{t}}), \tag{17.59}$$

$$\Gamma' = \Gamma(\mu) + \Gamma_{\mathrm{turb}}(\mu_{\mathrm{t}}). \tag{17.60}$$

The additional introduction of turbulent viscosity to the stress tensor in Eq. (17.60) is called the Reynold's stress tensor, while in the energy equation the fluctuating component increases the thermal diffusivity by a turbulent contribution (k_{turb}). The same correction appears in the conservation equations of chemical species, where the presence of a diffusion associated to fluctuations is introduced.

In particular, the conservation equation of the i-th chemical specie becomes the following:

$$\frac{\partial}{\partial t}(\rho Y_{\mathrm{k}}) + \nabla \cdot (\rho \mathbf{U} Y_{\mathrm{i}}) = -\nabla \cdot \left[\rho\left(\Gamma_{\mathrm{k}} + \frac{\mu_{\mathrm{t}}}{\mathrm{Sc}_{\mathrm{t}}}\right)\nabla Y_{\mathrm{k}}\right] + \dot{\Omega}_{\mathrm{k}}^{\mathrm{Chemistry}} + \dot{\Omega}_{\mathrm{k}}^{\mathrm{Spray}} + \dot{\Omega}_{\mathrm{k}}^{\mathrm{WallFilm}}, \tag{17.61}$$

where Sc_{t} is the turbulent Schmidt number defined as:

$$\mathrm{Sc}_{\mathrm{t}} = \frac{\mu_{\mathrm{t}}}{\rho \Gamma_{\mathrm{t}}}. \tag{17.62}$$

Determining the value of the turbulent viscosity μ_{t} is the main scope of the turbulence model. In the classical k-ε turbulence model, two transport equations are solved for the turbulent kinetic energy (k) and its dissipation rate (ε) to calculate the turbulent viscosity:

$$\mu_{\mathrm{t}} = \rho C_{\mu} \frac{k^2}{\varepsilon}, \tag{17.63}$$

where C_{μ} is a k-ε model parameter whose value is typically given as 0.09. The two transport equations are also characterized by the presence of constants which depend on the model and on the phenomena taken into account. The main drawback is that the dissipation rate of kinetic turbulent energy is constant for all the length scales. This is not very well representative of the reality and requires the adoption of particular functions to express the turbulence destruction near the walls, the so-called wall functions. These are used to express the gradient of the velocity when the mesh resolution is not adequately refined in the proximity of the walls. An improved formulation of the k-ε model (the RNG k-ε) adopts an expression for the source term of ε which is function of the strain rate [31]. This makes the model suitable for low Reynolds calculation and theoretically does not require the adoption of wall functions. The main drawback of this family of turbulence models, including also those based on a different formulation of the dissipation rate, such as the k-ω [32], is that turbulence is treated as an isotropic property of the flow. Flows inside of exhaust systems equipped with turbochargers and eventual mixers, to encourage the mixing between the injected reducing agent (ammonia or urea) and the gas stream, are characterized by strong swirl components. This highlights that turbulence may be an anisotropic property of the flow, which can be taken into account only resorting to the transport of the Reynolds stress tensor (Reynolds Stress Model) [33].

Particular care must be paid to the choice of the differencing scheme used for the solution of the governing equations. The choice is not univocal, since a trade-off between accuracy and computational cost exists. A first-order approximation for the convection term is the most stable approach, however if the target is the prediction of the mixing efficiency between ammonia and exhaust gas stream, then the solution will be affected by a significant amount of artificial viscosity, comparable to the turbulent one [33]. This issue can be overcome resorting to more refined calculation grids, which on the other end may lead to excessively long calculation time. The alternative is to adopt accurate differencing schemes, based on linear interpolation, along with TVD smoothing techniques to prevent the occurrence of spurious oscillations [28–30].

17.3.2 Modeling the UWS Injection

Since in SCR systems the urea/water solution is injected in the gas stream, additional submodels are needed to simulate the interaction between the liquid droplets and the exhaust gas. The most straightforward approach used in CFD for the simulation of spray injection is the Eulerian–Lagrangian method, which allows for detailed descriptions of individual droplets during their trajectories and their interaction with the continuous phase [24, 34]. The other possible way of modeling this aspect is the Eulerian–Eulerian approach. In this framework both the liquid and the gas phase are modeled with the same strategy, resorting to an Eulerian approach [35, 36]. The detailed resolution of the interaction between gas and liquid is much more accurate, however the computational effort is significantly higher, since it requires to discretize the injector hole and each single droplet, leading to very refined computational meshes. This main constraint is removed with the Eulerian–Lagrangian approach, where specific submodels are used to simulate the interaction between the liquid jet and the surrounding gas. The droplets injected in the gas are tracked with a Lagrangian approach and their motion is coupled to continuous phase motion via Newton's second law.

17.3.2.1 Spray Evolution

The spray droplets are described by stochastic particles which are usually referred as *parcels* [37]. Each parcel represents a class of identical, noninteracting droplets, and they are tracked through the physical space in a Lagrangian manner according to the mass, momentum, and energy exchange with the gas (Eulerian) phase. Additional phenomenological models are required to describe the various physical processes taking place in the subgrid length scales such as atomization, breakup, evaporation, heat transfer, turbulent dispersion, and collision. Spray atomization and breakup can be considered as the same process [38], atomization models are rarely used for simulation of urea/water solutions. Moreover, the low injection pressure used in injection systems (typically 6–9 bar) suggests that the droplet breakup occurs mainly due to the aerodynamic interaction between the droplet and the gas stream. For this reason, the droplet distribution can be imposed according to a certain random distribution of droplet diameters. A Rosin–Rammler law can be imposed to represent the distribution of droplet diameters at the injection point, assuming a known average diameter at the injection pressure typical of these systems [39]:

$$d_{\mathrm{p}} = d\left[-\ln(1-\xi)^{\frac{1}{n}}\right], \tag{17.64}$$

where d is the average diameter, ξ is a random number and $n = 1.21$ [39]. The secondary breakup, which accounts for the aerodynamic interaction between the liquid and the surrounding gas, can be modeled resorting to the WAVE model [38]. In this model the wavelength and growth rate leading to breakup are determined by a linear instability analysis performed on a cylindrical liquid jet of fixed radius, which penetrates through a circular orifice into a stationary incompressible gas environment. Liquid breakup can be described by postulating that new droplets are formed from a parent droplet with a radius proportional to the wavelength of the fastest growing or the most probable unstable surface wave.

Spray evaporation and heat transfer with the surrounding gas phase must be considered along with turbulent dispersion and droplet collisions [40].

Another important aspect that must be taken into account is how the spray interacts with the rigid walls present in the system. This is particularly important in SCR systems, since they are usually confined in limited space due to compactness requirements, therefore offering little space for spray penetration. The interaction between the spray parcels and the liquid film is modeled by the approach proposed by Stanton et al. [41]. The droplet impingement regimes are determined by the parameters describing the approaching droplets, the wall surface conditions, and the gas boundary layer characteristics in the near-wall region. The collision of a droplet with a liquid surface may result in sticking, spreading, bouncing, and splashing [42], as summarized in Fig. 17.8. The impingement regimes are identified by the Weber number We:

$$\mathrm{We} = \frac{\rho\left(\overrightarrow{V}_{\mathrm{P}}\overrightarrow{n}_{\mathrm{w}}\right)d_0}{\sigma}, \tag{17.65}$$

where $\overrightarrow{V}_{\mathrm{P}}$ is the relative velocity between the droplet and the wall and $\overrightarrow{n}_{\mathrm{w}}$ is the face normal of the impinging wall. The following transition criteria are used:

- $\mathrm{We} < 5$: stick
- $5 < \mathrm{We} < 10$: rebound
- $10 < \mathrm{We} < \mathrm{We}_{\mathrm{s}}$: spread
- $\mathrm{We} > \mathrm{We}_{\mathrm{s}}$: splash

We_{s} represents the splashing threshold and is given by [43, 44]:

$$\mathrm{We}_{\mathrm{s}} = (18)^2 d_0\left(\frac{\rho}{\sigma}\right)^{1/2}\left(\frac{\mu}{\rho}\right)^{1/4} f^{3/4}, \tag{17.66}$$

where ρ, σ, μ, d_0, and f are the droplet density, surface tension, dynamic viscosity, diameter at wall incidence, and frequency of droplet impingement on the film. The impact frequency is calculated in each boundary surface for each time step as:

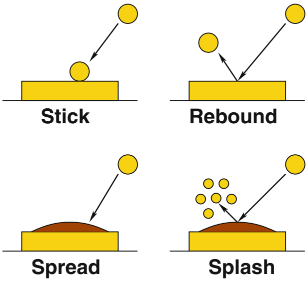

Fig. 17.8 Impingement regimes identified in the spray-wall impingement model

$$f = \frac{1}{\sum_{\mathrm{i}} {}^{N_{\mathrm{d,i}}}\!/_{\Delta t}}, \tag{17.67}$$

where $N_{\mathrm{d,i}}$ is the number of droplets contained in a single parcel and Δt is the time step. A detailed description of the correlations used for momentum and mass exchange between the droplets and the liquid film in the rebound and splash regimes can be found in [34, 43]. The splashing process is modeled by introducing three new droplets in the mesh for each impinging droplet.

17.3.2.2 Droplet Continuity Equation

The effect of evaporation of the liquid droplet is the only term that appears in the mass balance of a single liquid droplet. Its variation in time can then be expressed as:

$$\frac{\mathrm{d}m_{\mathrm{d}}}{\mathrm{d}t} = \dot{m}_{\mathrm{d}}, \tag{17.68}$$

where $\dot{m}_{\mathrm{d}}$ is the evaporation rate, calculated as a function of the droplet diameter D, of the liquid density ρ_{v}, of the mass diffusion coefficient Γ, and of the Sherwood number Sh:

$$\dot{m}_{\mathrm{d}} = -\pi D \Gamma \rho_v \mathrm{Sh} \ln\left(1 + \frac{X_{\mathrm{v,s}} - X_{\mathrm{v},\infty}}{1 - X_{\mathrm{v,s}}}\right). \tag{17.69}$$

The Sherwood number can be evaluated resorting to the formula proposed by Ranz-Marshall [45]:

$$\mathrm{Sh} = 2 + 0.6\,\mathrm{Re}^{1/2}\mathrm{Sc}^{1/3}. \tag{17.70}$$

The terms appearing as argument of the logarithm in Eq. (17.69) are the molar fractions of the species in the gas phase at a sufficiently far distance $X_{\mathrm{v},\infty}$ and the molar fractions at saturation. These terms are also used in a more compact form and referenced as the Spalding number B:

$$B = \frac{X_{\mathrm{v,s}} - X_{\mathrm{v},\infty}}{1 - X_{\mathrm{v,s}}}. \tag{17.71}$$

These correlations are valid only for evaporating droplets; different expressions must be considered when boiling occurs. In this case, the evaporation rate is governed by the rate of transfer between the droplet at temperature T_{d} and the gas at the temperature T needed to realize the phase change:

$$\frac{\mathrm{d}m_{\mathrm{d}}}{\mathrm{d}t} = -\frac{\pi D \lambda_{\mathrm{t}} \mathrm{Nu}}{c_{\mathrm{p,v}}} \ln\left(\frac{c_{\mathrm{p,v}}}{\hat{H}_{\mathrm{v}}}(T - T_{\mathrm{d}}) + 1\right), \tag{17.72}$$

where the Nusselt number is evaluated according to the following equation:

$$\mathrm{Nu} = 2 + 0.6\,\mathrm{Re}^{1/2}\,\mathrm{Pr}^{1/3}. \tag{17.73}$$

17.3.2.3 Droplet Motion Equation

From the Newton's law, the motion equation of the droplet can be stated as follows:

$$m_{\mathrm{d}} \frac{\mathrm{d}\mathbf{u}_{\mathrm{d}}}{\mathrm{d}t} = \mathbf{F}, \tag{17.74}$$

where $\mathbf{u}_{\mathrm{d}}$ is the droplet velocity and $\mathbf{F}$ is the resultant of the forces acting on it, namely the drag force and the gravity [39]:

$$\mathbf{F} = -\frac{\pi D^2}{8} \rho C_D |\mathbf{u}_{\mathrm{d}} - \mathbf{u}|(\mathbf{u}_{\mathrm{d}} - \mathbf{u}) + m_{\mathrm{d}}\mathbf{g}. \tag{17.75}$$

Other forces can be considered in order to take into account the lift resulting from the velocity gradient around the droplet or the virtual mass effect. However, in SCR simulations they can be neglected, since their contribution is usually from 2 to 3 order of magnitudes lower than the others [39]. A typical expression for the determination of the drag coefficient C_{D} is:

$$C_D = \begin{cases} \dfrac{24}{\mathrm{Re}_{\mathrm{d}}}\left(1 + \dfrac{1}{6}\mathrm{Re}_{\mathrm{d}}^{2/3}\right) & \mathrm{Re}_{\mathrm{d}} < 1000, \\ 0.424 & \mathrm{Re}_{\mathrm{d}} > 1000, \end{cases} \tag{17.76}$$

where Re_{d} is the Reynolds number of the droplet evaluated on the basis of the droplet-gas relative velocity:

$$\mathrm{Re}_{\mathrm{d}} = \frac{\rho |\mathbf{u}_{\mathrm{d}} - \mathbf{u}| D}{\mu}. \tag{17.77}$$

Alternative formulations can also take into account the effect of high volumetric fraction of liquid θ, which is a case typical of injections at low pressure [46]:

$$C_D = \begin{cases} \dfrac{24}{\mathrm{Re_d}}\left(\theta^{-2.65} + \dfrac{1}{6}\mathrm{Re_d^{2/3}}\theta^{-1.78}\right) & \mathrm{Re_d} < 1000 \\ 0.424 & \mathrm{Re_d} > 1000. \end{cases} \tag{17.78}$$

Furthermore, due to the interaction with the surrounding gas, the shape of the droplet can change and consequently also its drag coefficient. This aspect can be accounted for correcting the drag coefficient, according to what is proposed in several publications [47, 48] (Fig. 17.9).

17.3.2.4 Droplet Energy Equation

The energy balance of the droplet can be expressed referring to its sensible enthalpy H_d. The variation of the droplet sensible enthalpy is given by the convective heat exchanged with the surrounding gas and by the heat of evaporation required during the phase change:

$$m_\mathrm{d}\frac{\mathrm{d}H_d}{\mathrm{d}t} = \dot{m}_\mathrm{d}H_\mathrm{v}(T_\mathrm{d}) + \pi D\lambda_\mathrm{t}\mathrm{Nu}(T - T_\mathrm{d})f. \tag{17.79}$$

The corrective coefficient f takes into account the contemporary occurrence of heat and mass transfer. The Nusselt number is determined according to Eq. (17.73). By combining Eqs. (17.68) and (17.79), it is possible to determine the temperature of the droplet. In this process iterative procedures are usually adopted to determine unknown quantities, moreover the properties of the saturated vapor around the droplet are evaluated resorting to the one-third rule (Eq. 17.26).

17.3.2.5 Modeling the Urea/Water Solution

In this analysis, particular care must be paid to the way the urea–water solution is modeled. Several works have been published on the modeling of UWS injection, each of them resorting to specific simplifications of the problem [49–53]. The main source of uncertainty is the lack of characterization of urea–water solutions at various temperature levels. Additionally, the environment temperature at which UWS is injected is quite often critical for two reasons: the gas temperature is higher than the boiling temperature of the UWS droplet; the pipe wall temperature is higher than the boiling temperature of the droplet. These two conditions make the modeling of the UWS evaporation the major challenge in the simulation of SCR systems. By reviewing the literature in the field of UWS injection, it is found that the state of aggregation of urea is not clear during the evaporation of UWS. As a matter of fact, it can be varied among solid, molten and gas phases, depending on

Fig. 17.9 Droplet deformation due to the interaction with the surrounding gas

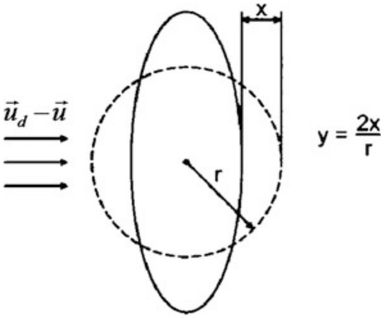

the local thermophysical conditions. In particular, the high gas temperature can be a source of a strong deviation from the so-called D^2-law of the droplet [54].

This is caused by the fact that the concentration of the two components in the solution changes during the evaporation, leading to possible high concentration of urea, which may result in formation of solid components. The result is a formation of a solid crust around the droplet which, due to the boiling of the inner liquid core, will cause a sudden explosion of the droplet when the inner pressure increases above a threshold level. Following the trajectory of a single UWS droplet, the history of the events taking places on its surface or inside its core can be determined. Considering that the melting point of urea is known to be around 406 K, at ambient temperature of 373 K only the water fraction evaporates from UWS droplet. At 423 K urea near droplet surface is expected to melt and thermally decomposes into ammonia and isocyanic acid. However, experimental observation reported that a vigorous gas evolution from molten urea commences at 425 K [51, 54]. Solidification can be observed after the complete depletion of liquid component from UWS. The deposits produced may be composed only by solidified urea, because the first urea-derived species, biuret, begins to be generated from the reaction of isocyanic acid with intact urea at 433 K. It has been demonstrated that modeling the radial distribution of temperature and urea concentration inside the droplet is not beneficial in terms of computational effort. Moreover, the comparison with rapid mixing models, in which temperature and concentration are assumed uniform over the droplet, does not show a significant improvement of accuracy [51]. When the temperature of the droplet is below the melting point of urea, the evaporation rate of urea can be modeled resorting to correlations available in the literature, which basically exploit the vapor pressure of solid urea [55]. Among all the proposed formulations, Bernhard et al. [56] characterized the vapor pressure extending the range of temperature above urea melting point, preserving a good matching of the formulation proposed by Krasulin [57]. In Fig. 17.10 it is shown the typical change of slope due to the initial evaporation of water and then to the gasification of urea followed by its immediate decomposition. Despite the different formulation of the vapor pressure, what emerges by the characterization of the UWS droplet is the low evaporation rate of urea if compared to water. This

Fig. 17.10 Two phases of the D^2-*law* during evaporation of a UWS droplet at ambent temperature of 423 K [54]

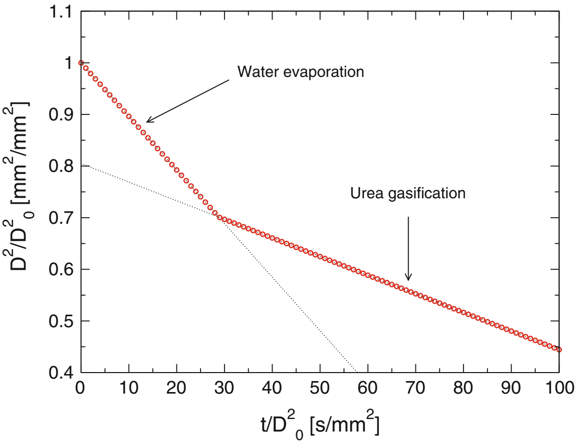

aspect, combined with the need of having compact mixing devices, results in a frequent formation of liquid film with a higher concentration of urea than the injected liquid.

17.3.3 Modeling the Formation of Liquid Film

Once the trajectory of each single droplet is known, it is possible to evaluate its interaction with the walls included in the calculation domain. The definition of the impingement regimes presented in the previous section allows to know the net amount of mass that will form a liquid film over the walls. The interaction between spray and the wall can be realized defining specific solution fields on the surfaces where the formation of liquid film is likely to occur. These allow to define scalar and vectorial fields for the solution of the conservation equations of mass, momentum end energy [43, 58, 59]. The coupling between spray and wall film models can be realized resorting to the definition of a finite area field [60], over which the integration of the differential operations can be performed in a similar way to the finite volume approach. Within this framework, a schematic representation of a thin liquid film on a curved surface can be represented as in Fig. 17.11, where it is possible to identify a curved wall surface S_w, with its normal $\mathbf{n}$, a free surface of the liquid film S_{fs}, a liquid film of thickness h and an assumed velocity profile $\mathbf{v}$, varying from zero at the wall to the free surface velocity $\mathbf{v}_{fs}$.

In order to derive the governing equations for the liquid film, the following assumptions regarding the wall film behavior can be made:

- the film is thin enough for the boundary layer approximation to apply, i.e., the spatial gradients of the dependent variables tangential to the surface are negligible compared to those in the normal direction;

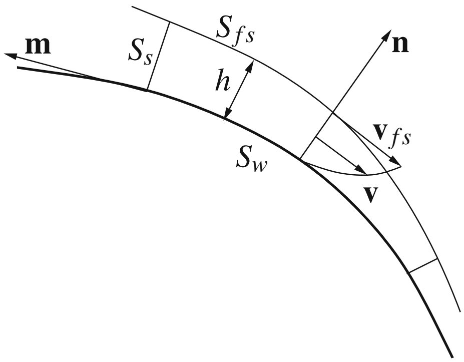

Fig. 17.11 Schematic representation of a thin liquid film

- film motion is caused by the spatial variation in the tangential direction of the total pressure p_L, shear at the wall and film interface, tangential momentum sources provided by incoming droplets, and body forces (e.g., gravity acceleration);
- under boundary layer approximations, local liquid pressure p_L within the film can be taken to be constant across the film depth;
- liquid pressure p_L consists of the following components: pressure of the surrounding gas p_g; droplet impact pressure p_d; capillary (or Laplace) pressure p_σ; and hydrostatic pressure p_h. Thus, the liquid film is locally subject to the following pressure:

$$p_\mathrm{L} = p_\mathrm{g} + p_\mathrm{d} + p_\sigma + p_\mathrm{h}. \tag{17.80}$$

- the tangential momentum lost by the incident droplets provides a source of tangential momentum to the wall film;
- the mass flux due to incident droplets may be represented by a spatially smoothly varying function, so that conventional differential operations apply.

Using the above-mentioned modeling assumptions, the general liquid film governing equations can be derived in the following way:

$$\int\limits_{S_\mathrm{w}} \frac{\partial h}{\partial t}\mathrm{d}S + \oint\limits_{\partial S_\mathrm{w}} h\mathbf{m}\cdot\bar{\mathbf{v}}\mathrm{d}L = \int\limits_{S_\mathrm{w}} \frac{\dot{m}_\mathrm{S}}{\rho_\mathrm{L}}\mathrm{d}S + \int\limits_{S_\mathrm{w}} \frac{\dot{m}_\mathrm{V}}{\rho_\mathrm{L}}\mathrm{d}S, \tag{17.81}$$

where h is the local liquid film height, $\bar{\mathbf{v}}$ is the height average liquid film velocity tangential to the surface, ∂S_w is the boundary line of the surface S_w, $\mathbf{m}$ is the unit normal vector to the line ∂S_w, which is at the same time tangential to the surface S_w, ρ_L is the liquid film density, $\dot{m}_\mathrm{S}$ is the mass source surface density, and $\dot{m}_\mathrm{V}$ is the mass evaporating from the film. Referring to the single face area, the film continuity equation can be expressed as a function of the film thickness, since the assumption of incompressible fluid is valid:

$$\frac{\partial h}{\partial t} + \nabla\cdot(h\mathbf{U}_\mathrm{f}) = S_\mathrm{M} + S_\mathrm{V}. \tag{17.82}$$

The last term S_V accounts for film evaporation under both dynamic and thermal effects [58]. Since the impinging liquid spray is multicomponent (water and urea in our case), species tracking must be considered in the film. A set N_S-1 of conservation equations must be solved, where N_S in the number of chemical components considered:

$$\frac{\partial h Y_{f,k}}{\partial t} + \nabla \cdot \left(h \mathbf{U}_f Y_{f,k} \right) = S_{M,k} + S_{V,k}, \tag{17.83}$$

where $Y_{f,k}$ indicates the mass fraction of the k-th specie. The two terms $S_{M,k}$ and $S_{V,k}$, are the amount of the k-th species entering the film due to the spray impact and leaving the film due to evaporation, respectively. Similarly, the liquid film momentum equation can be formulated:

$$\frac{\partial h \mathbf{U}_f}{\partial t} + \nabla \cdot \left(h \mathbf{U}_f \mathbf{U}_f \right) = -\frac{1}{\rho_f} \nabla (h p_f) + \tau_g - \tau_w + h\mathbf{g} + \mathbf{S}_U, \tag{17.84}$$

where τ_{fs} is the tangential viscous force at the free surface, τ_w is the tangential viscous force at the wall, $\mathbf{g}_t$ is the tangential component of gravity acceleration, $\nabla_s p_L$ is the surface gradient of the pressure and $\mathbf{S}_v$ is the tangential component of the momentum source from incoming droplets. In SCR systems the urea–water solution is usually injected in the gas stream without undergoing a heating process, so its temperature is close to the ambient one. Because of this, the impinging jet is heated by the gas stream and then by the contact with the pipe walls or with the mixer blades. In compact systems, typical of automotive applications, the droplet heat up before the impact with rigid walls is not enough to get all the liquid component evaporated. The process is therefore completed after the impact with the walls and is governed by two phenomena: the heating of the liquid film and the cooling of pipe walls due to the impingement of a colder liquid. This interaction can be taken into account solving for the energy balance of the liquid and the walls. The energy equation of the liquid film is expressed once again as a function of the sensible enthalpy:

$$\frac{\partial h H_{s,f}}{\partial t} + \nabla \cdot \left(h \mathbf{u}_f H_{s,f} \right) = j_g - j_w + S_H, \tag{17.85}$$

where the source terms are the contribution due to: the heat flux exchanged with the gas (j_g), the heat flux due to conduction between the liquid and the pipe walls (j_w), and the enthalpy associated with the net mass of the droplet entering the liquid film (S_H). The film-gas heat flux terms accounts for the contribution of the temperature gradient (j_s) with the addition of the heat flux required by the evaporation ($S_V h_{v,\,f}$):

$$j_g = \frac{\lambda_{t,l}}{\rho_f} \frac{\partial T}{\partial n}\bigg|_{z=h} + S_V h_{v,f} = j_s + S_V h_{v,f}. \tag{17.86}$$

The conductive heat flux is determined by assuming a parabolic profile of the temperature within the liquid film [58]:

$$j_{\mathrm{w}} = 3\frac{\lambda_{\mathrm{t,l}}(T_{\mathrm{f}} - T_{\mathrm{w}})}{\rho_{\mathrm{f}} h} - \frac{1}{2} j_{\mathrm{g}}. \tag{17.87}$$

The energy balance of the pipe walls takes into account the conduction heat that occurs inside the material and is coupled to the liquid film energy balance by means of the j_{w} term. Once the thermal properties of the walls are known, the balance can be expressed referring to the temperature of the material:

$$\rho_{\mathrm{w}} c_{\mathrm{w}} \frac{\partial T_{\mathrm{w}}}{\partial t} - \lambda_{\mathrm{t,w}} \nabla^2 T_{\mathrm{w}} = \frac{j_{\mathrm{w/g}} \rho_{\mathrm{f}}}{\delta}. \tag{17.88}$$

This variation depends on the thermal capacity of the pipe wall material, and in general is very limited if only a narrow time interval is modeled. For steady-state simulation the thermal capacity can be reduced by an arbitrary factor, in order to speed up the thermal transient. However, if pulsating injection is modeled, this strategy cannot be adopted and the time interval to model must be large, in order to observe a significant temperature variation. The coupling with the solid wall balance can be realized resorting to fluid structure interaction approaches, where proper algorithms for coupling the solution matrices must be adopted, or resorting to the definition of a finite area field representing the wall temperature. The heat flux between the liquid film and the pipe walls is calculated resorting to the heat conduction theory. In particular, inside SCR systems it may happen that the wall temperature is much higher than the liquid film temperature (especially when a liquid spray is approaching a dry surface), resulting in what is called the Leidenfrost regime. In this condition, a vapor cushion is formed between the film and the wall, causing a drop in the heat exchange coefficient. The calculation of the heat flux must therefore be corrected in order to take into account this particular phenomenon [61]. However, this correction may not be enough for the prediction of the liquid film dynamics, since it affects mainly the thermal balance. A correction of the momentum exchange between the liquid layer and the pipe walls must be accounted for, in order to reproduce the reduced friction coefficient caused by the vapor gap.

17.3.4 Discretization of Source Terms and Equations

Referring to the liquid film continuity Eq. (17.82), the source term related to the arrival of droplets can be determined as:

$$S_{\mathrm{M}} = \frac{4\pi\rho_{\mathrm{d}}}{3A\rho_{\mathrm{f}}\Delta t} \sum_{\mathrm{i}=1}^{N_{\mathrm{d}}} r_{\mathrm{i}}^3, \tag{17.89}$$

where the amount of mass considered is given by the net number of droplets designated to remain in the liquid film. The term S_{V} is related to the evaporation rate of each component of the liquid film. It can be expressed in two different ways on the basis of the flow regime:

- when dynamic effects are prevailing (high flow stream velocity):

$$S_{\mathrm{V,k}} = \frac{|\tau_{\mathrm{g}}|}{\rho_{\mathrm{f}}|\mathbf{u}_\infty - \mathbf{u}_{\mathrm{s}}|}\left((B_k+1)^{1/\mathrm{Sc_k}}-1\right); \tag{17.90}$$

- when thermal effects are prevailing (high gas temperature):

$$S_{\mathrm{V,k}} = \frac{j_{\mathrm{s}}}{\rho_{\mathrm{f}} c_{\mathrm{p}} (T_\infty - T_{\mathrm{s}})}\left((B_k+1)^{1/\mathrm{Le}_k}-1\right). \tag{17.91}$$

Once again, the ∞ subscript indicates the gas condition at far field from the liquid film, whereas the condition s refers to quantities evaluated at the film surface using the one-third rule. The specific heat capacity c_{p} is evaluated with the one-third rule, whereas Le indicates the Lewis number defined as the ratio between the thermal diffusivity and the molecular diffusivity. This number can be also expressed as the ratio between Prandtl and Schmidt numbers:

$$\mathrm{Le} = \frac{\mathrm{Sc}}{\mathrm{Pr}}. \tag{17.92}$$

All these equations are valid for evaporating liquid film regimes. When boiling occurs an additional term, evaluated on the basis of the first principle of thermodynamics, needs to be added. The overall evaporation rate can be derived from the evaporation rate of each single component:

$$S_{\mathrm{V}} = \sum_{k=1}^{N_{\mathrm{f,C}}} S_{\mathrm{V},k}. \tag{17.93}$$

The source term in the film momentum equation is considered to account for the interaction between the impinging spray and the pre-existent liquid film. This is particularly important in SCR systems, since the spray axis is alway angled with respect to the normal direction of the pipe and mixer walls. For this reason, the contribution to the film momentum can be decomposed into two components: one normal to the wall surface and the other one tangential ($\underline{t}$), laying on the same plane of the face representing the wall. The former can be included in the film pressure equation, since it acts as an increase of pressure due to the canceling of the momentum in that direction. The latter, instead, is considered in the momentum equation as follows (S_{U}):

$$\mathbf{S}_{\mathrm{U}} = \frac{4\pi\rho_{\mathrm{d}}}{3A\rho_{\mathrm{f}}\Delta t}\sum_{i=1}^{N_{\mathrm{d}}} r_{\mathrm{i}}^3(\mathbf{u}_{\mathrm{i}}\cdot\underline{t})\underline{t}. \tag{17.94}$$

Concerning the film energy conservation equation, the contribution of the sensible heat of the impinging droplet depends on the temperature of the droplet itself:

$$S_{\mathrm{H}} = \frac{4\pi\rho_{\mathrm{d}}}{3A\rho_{\mathrm{f}}\Delta t}\sum_{i=1}^{N_{\mathrm{d}}} r_{\mathrm{i}}^{3}\hat{H}_{\mathrm{d},i}, \tag{17.95}$$

where $\hat{H}_{d,i}$ is the specific sensible enthalpy of the droplet.

From a numerical point of view, it is convenient to write the liquid film governing equations in a general surface integral form as:

$$\frac{\mathrm{d}}{\mathrm{d}t}\int_{S} h\Phi\,\mathrm{d}S + \oint_{\partial S} h\mathbf{m}\cdot\overline{\mathbf{v}}\Phi\,\mathrm{d}L = \int_{S} s_{\Phi}\,\mathrm{d}S, \tag{17.96}$$

where Φ represents a generic scalar or vectorial quantity and s_{Φ} is the source term. This surface transport equation (Eq. 17.96) is discretized using the Finite Area Method (FAM) on a surface unstructured mesh consisting of arbitrary polygonal control areas. Figure 17.12 shows a sample polygonal control area S_{P} around the computational point P located in its centroid, the edge e, the edge length L_{e}, the edge unit bi-normal vector $\mathbf{m}_{\mathrm{e}}$, and the centroid N of the neighboring control area sharing the edge e. The bi-normal $\mathbf{m}_{\mathrm{e}}$ is perpendicular to the edge normal $\mathbf{n}_{\mathrm{e}}$ and to the edge vector $\mathbf{e}$. Applying a second-order collocated FAM, Eq. 17.96 can be discretized on the control area S_{P} (see Fig. 17.12) as follows:

$$\frac{\mathrm{d}(h_{\mathrm{P}}\Phi_{\mathrm{P}}S_{\mathrm{P}})}{\mathrm{d}t} + \sum_{\mathrm{e}} h_{\mathrm{e}}\mathbf{m}_{\mathrm{e}}\cdot\mathbf{v}_{\mathrm{e}}L_{\mathrm{e}}\,\Phi_{\mathrm{e}} = (s_{\Phi})_{\mathrm{P}}S_{\mathrm{P}}, \tag{17.97}$$

where the subscripts P and e represent the face-center and the edge-center values. The edge-center value of the dependent variable Φ is calculated using the following linear interpolation formula:

$$\Phi_{\mathrm{e}} = (\mathbf{T}_{\mathrm{e}})^{T}\cdot\left[e_{x}\mathbf{T}_{\mathrm{P}}\cdot\Phi_{\mathrm{P}} + (1-e_{x})\mathbf{T}_{\mathrm{N}}\cdot\Phi_{\mathrm{N}}\right]. \tag{17.98}$$

where e_{x} is the interpolation factor, which is calculated as the ratio of the geodetic distances $\overline{eN}$ and $\overline{PeN}$ (Fig. 17.12):

$$e_{x} = \frac{\overline{eN}}{\overline{PN}}, \tag{17.99}$$

and T_{P}, T_{N}, and T_{e} are the tensors of transformation from the global Cartesian coordinate system to the edge-based local coordinate system defined in Fig. 17.13. Dependent variables in the convection term in Eq. (17.97) can be discretized using interpolation methods which locally blend linear and upwind interpolation schemes in order to preserve boundedness. The temporal discretization is performed by using the first-order accurate Euler implicit scheme [28].

Liquid film governing equations are solved using the segregated solution procedure, where the two equations are separately solved and coupling is recovered through the iterative procedure.

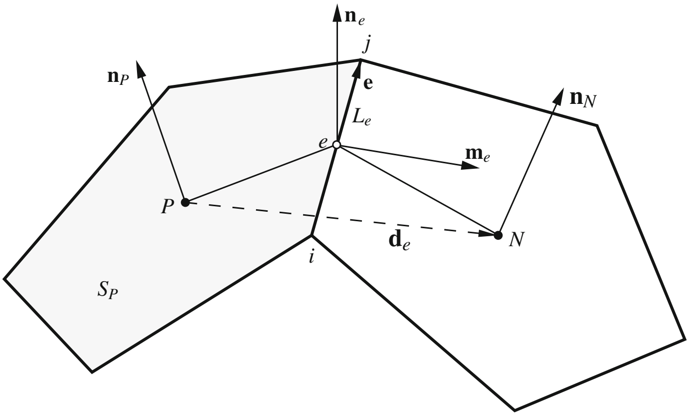

Fig. 17.12 Polygonal control area

17.3.5 Examples of CFD Application

All the submodels presented in the previous subsections have been implemented in an open source CFD code, OpenFOAM® [62], in order to show the potentialities of a CFD analysis of the exhaust system equipped with urea injection device. Most often, the prediction of a CFD calculation may be erroneously considered as the truth of what is happening at a certain scale level. Unfortunately, this misinterpretation may lead to wrong considerations in the case the prediction exactly matches some experimental results (obtained directly or indirectly), hence one may assume that it tells the truth, or in the case it does not match exactly the experimental measurement, hence judging that the model does not capture the physics correctly. Considerations drawn from the analysis of the calculated results, must be seen at the light of captured trend instead of exact value matching. In first place, every model for the simulation of a complex process, such as the injection of a multicomponent liquid phase into a hot gas stream, is based on simplifications, otherwise the fully detailed modeling of the phenomena would be much more expensive than the experimental testing of several prototypes. In second place, the experimental measure is usually carried out indirectly, hence hiding the effects that other phenomena may introduce in the overall process. In particular, the quality of the mixing between the ammonia, generated by the thermal decomposition of the injected urea, and the gas stream is indirectly measured by the abatement efficiency of the SCR catalyst, because of the 1 to 1 molar ratio between ammonia and nitrogen oxides. This direct correlation neglects the eventual impact of solid deposit formation during the operating conditions, or the deposition of liquid droplets onto the catalyst surface.

Additionally, CFD simulations are carried out considering steady-state simulation of both the UWS injection and mixing devices, imposing steady-state boundary conditions corresponding to averaged mass flow and temperature values.

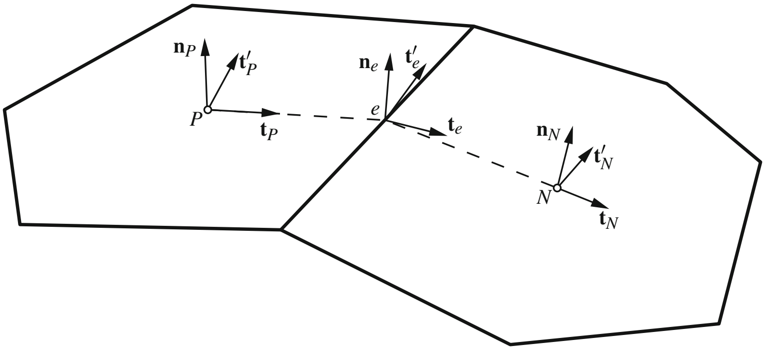

Fig. 17.13 Edge-based local coordinate system

This is obviously far from what happens inside of an exhaust system, when the IC engine is mounted on the test bench. The pulsating flow coming from the cylinders, together with discontinuities in the gas composition and temperature, may affect the global mixing efficiency. For this reason, an important perspective of simulation can be sought in the usage of time varying boundary conditions or in the adoption of hybrid models in which 1D and 3D codes are fully integrated [63]. In this section, the applications of a CFD model to simple test cases is presented, in order to highlight the aspects that can be investigated. In particular, in order to compare the calculation results with similar calculations performed with a different CFD tool, the test case modeled by Strom [39], has been analyzed. The case chosen for the comparison is the one with the highest volumetric flow (100 m/s) at the highest gas temperature (573 K), in order to easily highlight the behavior of gas stream and droplets. In Fig. 17.14a, b the droplet diameter and temperature are displayed, respectively. It is shown that the droplets with the smallest diameter are easily dragged by the gas stream, as they remain confined in the upper region of the pipe, whereas the droplets with larger diameter preserve their momentum, showing a lower deviation from the injection direction. The small droplets, instead, are characterized by a velocity close to that of the gas stream (Fig. 17.15) and are heated up more quickly.

The quicker heat up of the smallest droplets leads to an evaporation of the water fraction of each droplet. This is visible in Fig. 17.16a, b, where the droplets with the largest diameter show a negligible evaporation of both water and urea. As the droplet size decreases, the quicker heat up leads to an almost complete evaporation of the water fraction. Since the droplet temperature is lower than the urea thermal decomposition threshold, the evaporation of urea is very limited, hence the fraction of urea tends to unity. As previously described, the urea fraction of each single droplet evaporates with a rate close to the solid urea sublimation. The gaseous urea is then thermally decomposed with the rate described in Eq. (17.36). The integration of the chemistry has been performed resorting to an ODE solver based on the SIBS algorithm [64] according to what has been described in the section

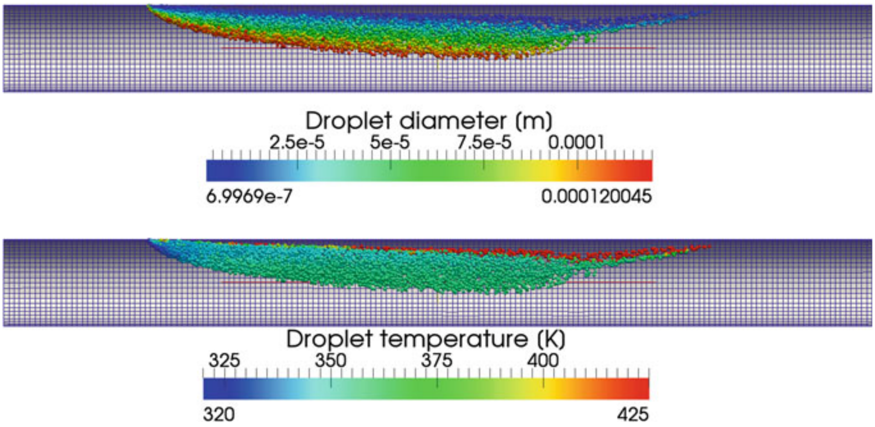

Fig. 17.14 UWS spray: droplet diameter and temperature distribution

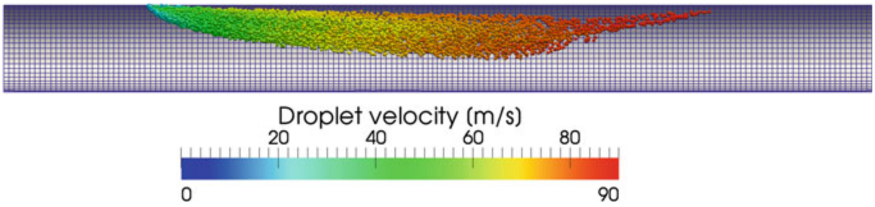

Fig. 17.15 UWS spray: droplet velocity distribution

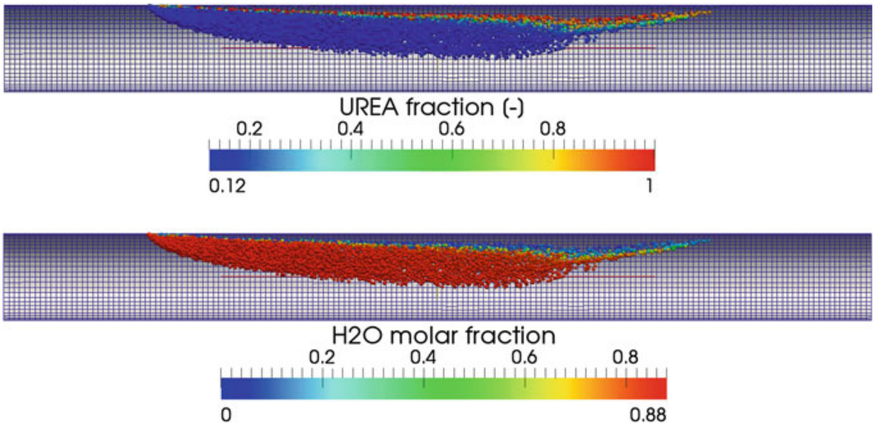

Fig. 17.16 UWS spray: urea and water molar fraction inside the droplets

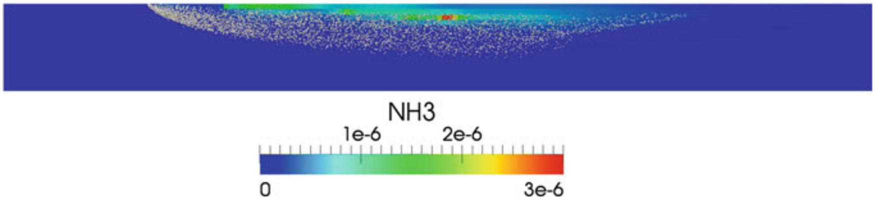

Fig. 17.17 Ammonia mass fraction in the gas stream

relative to 1D models. In Fig. 17.17, it is displayed the gaseous mass fraction of ammonia resulting from the thermal decomposition of the evaporated urea. As can be seen, the ammonia produced is confined in the upper region of the pipe, as a consequence that only the small droplets are likely to evaporate quickly. This aspect suggests that at high flow conditions the presence of the mixer is fundamental to have a uniform distribution of ammonia at the inlet of the catalyst.

Considering that the test case modeled has a length of 1 meter, it is evident that, even considering the most favorable condition for complete evaporation, namely high mass flow rate and gas temperature, the length required for complete evaporation is not enough. This consideration indicates that in real engine applications the space available to complete evaporation is usually not sufficient due to compactness issues. This justifies the adoption of a mixer, placed either upstream or downstream of the injection point, as a device to increase the turbulence intensity in the gas stream, so that the droplet-gas mass transfer and the gaseous species mixing are enhanced. As a secondary effect, the presence of the mixer favors the wall-droplet interaction, in order to generate smaller droplets when the impact occurs and to improve the evaporation rate by the formation of a liquid film. Therefore, in real applications an important role is played by the liquid film layer formed onto the pipe surface and on the mixer blades. The validation of liquid film models is very difficult to be performed, since in the literature there are few works about this topic with a detailed experimental characterization [65]. In particular, the approach presented has been validated for the case of a single component liquid spray designed for port fueled spark ignition engines [66]. In this section it is presented a simple test case which shows the dynamics of the interaction between the UWS spray and the pipe walls, highlighting the contribution to the evaporated urea coming from the spray and from the liquid film. To reproduce realistic operating conditions, the spray injection is directed with a angle of 45 ° with respect to the pipe axis. The operating conditions are summarized in Table 17.1. In particular, a null mean flow condition was taken into account in order to facilitate the analysis of the results. After the injection, the UWS spray reaches the pipe wall opposite to the injection section, where the formation of the liquid film layer occurs. Assuming this instant as the time 0, Fig. 17.18a, b show the evolution of the liquid film thickness during the first 15 ms. In particular, the liquid layer is spread along the pipe axis due to the momentum of the impinging

Table 17.1 Initial conditions test in the calculations

Injection pressure (bar)	8.52
Injection velocity (m/s)	37.701
Injection temperature (K)	300
Gas temperatures (K)	550
Wall temperature (K)	550
Wall heat specific capacity (J/m^{3}K)	3,532,500
Wall heat conductivity (W/mK)	18
Wall thickness (m)	0.002
Pipe diameter (m)	0.05

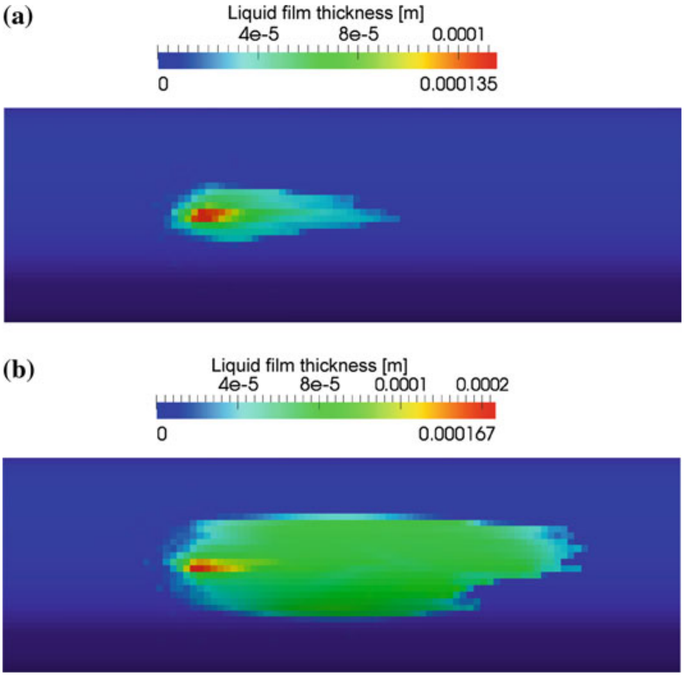

Fig. 17.18 Liquid film thickness during the UWS injection: **a** 0 ms, **b** 15 ms

liquid droplets. The highest film section is reached in the region where the incident spray impacts on the film.

When the droplet enters the liquid film, it brings a momentum source but also a contribution to the energy balance of the film itself. In Fig. 17.19a, b it is shown the temperature of the liquid film at two different times. The coldest region lays in the point where the cold spray core reaches the wall. The temperature of the spray remains close to the injection temperature, due to the short space and time available to realize a significant heat up of the droplet. The peripheral regions of the liquid film are characterized by a low layer thickness, ending up in a quicker

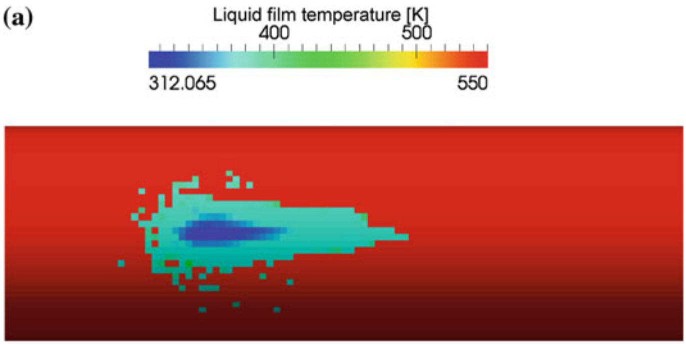

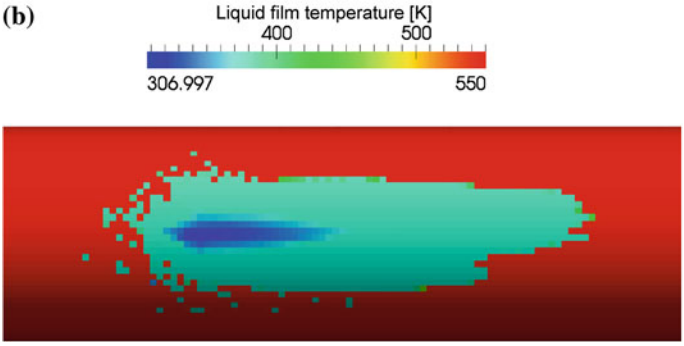

Fig. 17.19 Liquid film temperature at two different times: **a** 5 ms, **b** 20 ms

Fig. 17.20 Visualization of the temperature level of the liquid fraction inside the computational domain after 20 ms: spray and wall film

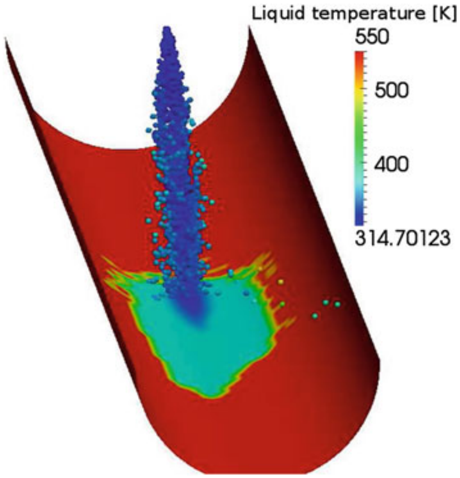

heating due to the heat exchanged with the surrounding gas and the pipe walls. A narrow spray cone angle (14 deg) has been imposed, in order to have a high impact frequency, resulting in an impact regime confined within the splash and spread regimes. The formation of liquid film is therefore immediate and the average temperature at which the droplets hit the wall surface is around 320 K, meaning that there is an increase of temperature of about 20 K (mainly determined by the small droplets). Figure 17.20 shows the temperature of the liquid fraction in the calculation domain, namely the spray and the liquid film. The size of the droplets is not scaled with the diameter, they have all the same size, in order to highlight the temperature at which the impact occurs. It can be seen that the spray core is the portion at the lowest temperature, while the particles at higher temperature are those characterized by a small diameter, as a result either of the injection model or of the splashing regimes occurring. The wall temperature, assuming for simplicity sake that the pipe is adiabatic with respect the external environment, shows a consistent cooling in the region where the liquid jet core hits the wall surface (Fig. 17.21a, b). Considering the limited time simulated, the effect of wall thermal conductivity can be neglected, since it is characterized by a higher characteristic time. The portion of the surface covered by the dragged liquid film remains at a higher temperature, since the liquid has been heated by the wall during its path along the pipe and therefore the cooling effect is weaker than in the region where the impingement occurs. Moreover, in all these observations it has to be considered that the film is heated also by the surrounding air via convection. The combination of all the effects results in the determination of the evaporation rate, which shows that the main contribution to the production of water and urea in gaseous phase is the evaporation of the liquid film. As shown in Fig. 17.22a, b, where the thermal decomposition of urea has not been modeled, after 15 ms it is evident that both gaseous water and urea are produced by the evaporation of the liquid film, whereas the contribution of the spray is almost negligible, especially for urea. Additionally, the two figures show how the profile of the two species is identical with different values of mass fractions, due to the lower evaporation rate of urea. Referring to a real engine configuration (Fig. 17.23), it appears evident how limited is the space available to the spray to completely evaporate. Following the trajectory of the UWS droplets, once again it can be noted that the smallest droplets are strongly deflected from the direction of the nozzle axis. These droplets then undergo a heating process, ending their trajectory by hitting the mixer walls. The large diameter droplets, instead, hit the mixer walls in the lower region due to the weaker deflection caused by their higher inertia. Figure 17.23 shows also the difference between the urea produced by the spray and by the liquid film. In particular, the yellow cloud represents the urea evaporated from the liquid film, whereas the red one represents the portion coming from the spray. Both the clouds have been plotted thresholding the two fields with the same minimum value. Once again, the result indicates that the major contribution to the urea, hence ammonia, production comes from the liquid film. The small contribution of the spray is mainly due to the small droplets that are recirculated by the vortexes originated at the sharp edges of the geometry. These droplets remain trapped in the recirculation vortex and therefore have enough time to heat up and evaporate.

The final purpose of the UWS injection and its mixing with the gas stream is the need of having an homogeneous distribution of ammonia at the catalyst inlet. As

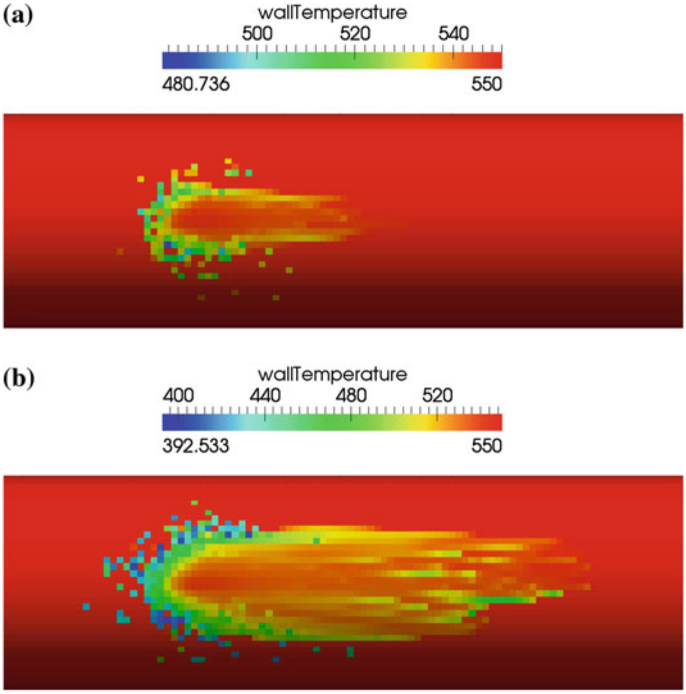

Fig. 17.21 Wall temperature during UWS the injection: **a** 0 ms, **b** 15 ms

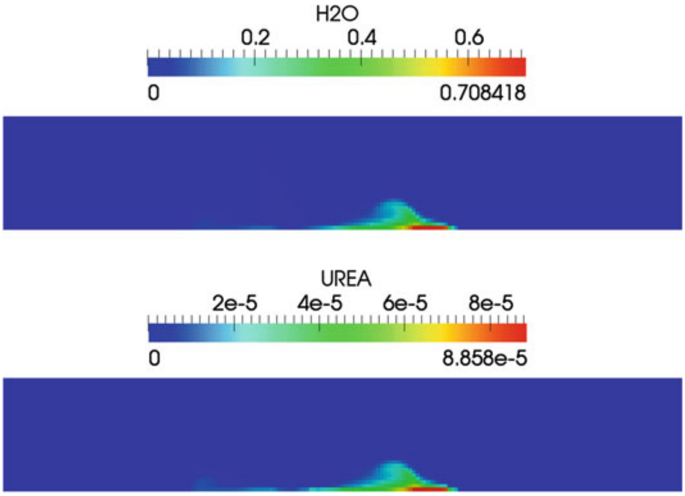

Fig. 17.22 Evaporated mass fraction of water and urea during the UWS injection

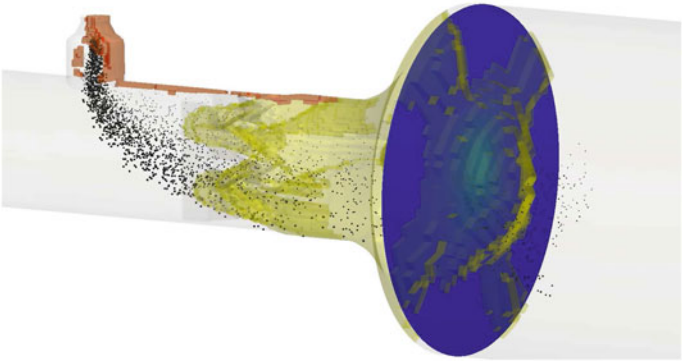

Fig. 17.23 Distinction between urea produced by the evaporation of the spray and by the evaporation of the liquid film

anticipated, the 1 to 1 molar ratio between ammonia and nitrogen oxide, required by the standard SCR reaction, implies that regions in the gas stream, where the concentration of ammonia is low, keep their content of nitrogen oxides. This fact correlates the catalyst efficiency to the degree of uniformity of the reducing agent, namely ammonia. This strong link facilitates the optimization of the SCR systems, since it is enough to estimate how uniform is the distribution of ammonia at the catalyst inlet to know if the system can operate efficiently or not. The level of ammonia distribution uniformity can be determined by the CFD analysis, resorting to different definitions a uniformity index. The most used formulation of the uniformity index is based on the probing and averaging of the mass fraction of ammonia along a surface at the inlet of the catalyst [67, 68]:

$$\mathrm{UI} = 1 - \frac{\sum_{\mathrm{i}} \left| Y_{\mathrm{NH_3,i}} - \overline{Y}_{\mathrm{NH_3}} \right| A_{\mathrm{i}}}{2 \sum_{i} Y_{\mathrm{NH_3,i}} A_{\mathrm{i}}}, \tag{17.100}$$

where $Y_{\mathrm{NH_3,i}}$ indicates the local value of the mass fraction of ammonia at the face center of a sample surface upstream of the catalyst, while $\bar{Y}_{\mathrm{NH_3}}$ is the average value of the ammonia mass fraction over the sampling surface. In case of ammonia equally distributed over the sampling surface, the index would reach the unity, whereas a peak of ammonia localized in a small portion of the sampling surface would lead to values close to zero. The calculation of this index must be performed over a planar surface parallel to the one representing the catalyst inlet, requiring that the mesh of the domain is oriented accordingly and possibly hexahedral. In case the mesh contains tetrahedral elements, and consequently does not allow for the definition of such surface, surface cutting techniques together with field interpolation must be adopted.

References

1. P. Forzatti. Present status and perpectives in de-NO$_x$ catalysis. *Applied Catalysis*, 222:221–236, 2001.
2. G. Montenegro and A. Onorati. 1d thermo-fluid dynamic modelling of de-nox scr systems for diesel engine exhaust gas after-treatment. *Int. J. of Vehicle Design*, 41(No.1/2/3/4):285–306, 2006.
3. G. Montenegro and A. Onorati. 1d thermo-fluid dynamic modeling of reacting flows inside three-way catalytic converters. *SAE International Journal of Engines*, 2(1):1–16, 2009.
4. A. Onorati, G. Ferrari, G. D'Errico, and G. Montenegro. The prediction of 1d unsteady flows in the exhaust system of a si engine including chemical reactions in the gas and solid phase. *SAE Technical Paper, SAE Transactions J. Engines*, pages 01–0003, 2002.
5. J. Wurzenberger, G. Auzinger, R. Heinzle, and R. Wanker. 1d modelling of reactive fluid dynamics, cold start behavior of exhaust systems. *SAE Technical Paper*, 2006-01-1544, 2006.
6. T. Morel, J. Silvestri, K. Goerg, and R. Jebasinski. Modeling of engine exhaust acoustics. *SAE Technical Paper*, 1999-01-1665, 1999.
7. A. Onorati, M. Perotti, and S. Rebay. Modelling one-dimensional unsteady flows in ducts: Symmetric finite difference schemes versus galerkin discontinuous finite element methods. *International Journal of Mechanical Sciences*, 39(11):1213–1236, 1997.
8. D. E. Winterbone and R. J. Pearson. *Theory of engine manifold design*. Professional Engeneering Publishing, London, 2000.
9. A. Burcat and B. Ruscic. Third Millennium Ideal Gas and Condensed Phase Thermochemical Database for Combustion with Updates from Active Thermochemical Tables. *Report TAE960*, 2005.
10. R. W. MacCormack. A numerical method for solving the equations of compressible viscous flow. *AIAA*, 81-0110, 1981.
11. P. D. Lax and B. Wendroff. Systems of conservation laws. *Comm. Pure Appl. Math.*, 13:217–237, 1960.
12. M. Chapman, J. M. Novak, and R. A. Stein. Numerical modeling of inlet and exhaust flows in multi-cylinder internal combustion engines. *ASME Winter Annual Meeting*, 1982.
13. G. Montenegro, A. Della Torre, A. Onorati, R. Fairbrother, and A. Dolinar. Development and application of 3d generic cells to the acoustic modelling of exhaust systems. *SAE 2011 Noise and Vibration Conference and Exhibition*, 2011-01-1526, 2011.
14. E. Jean, V. Leroy, G. Montenegro, A. Onorati, and Laurell. M. Impact of ultra low thermal inertia manifolds on emission performance. *SAE Technical Paper*, 2007-01-0935, 2007.
15. S. W. Churchill. Comprehensive Correlating Equations for Heat, Mass and Momentum Transfer in Fully Developed Flow in Smooth Tubes. *Ind. Eng. Chem. Fundam.*, 16:109–116, 1977.
16. S. W. Churchill. Friction-Factor Equation Spans all Fluid Flow Regimes. *Chem. Eng.*, pages 91–92, 1977.
17. R. J. Clarkson and S. F. Benjamin. Modelling the Effect of Moisture on Catalyst Warm-Up. *IMechE*, 1995.
18. S. H. Chan and D. L. Hoang. Chemical Reactions in the Exhaust System of a Cold-Start Engine. *Chem. Eng. Technol.*, 8:727–730, 2000.
19. S. Heller and G. Wachtmeister. Analysis and modeling of heat transfer in the si engine exhaust system during warm-up. *SAE Technical Paper*, 2007-01-1092, 2007.
20. S.M. Ghiaasiaan. *Two-Phase Flow, Boiling, and Condensation: In Conventional and Miniature Systems*. Cambridge University Press, 2007.
21. Y. Taitel and A.E. Dukler. A model for predicting flow regime transitions in horizontal and near horizontal gas-liquid flow. *AIChE Journal*, 22(1):JANUARY, 1976, 1976. cited By (since 1996) 282.

22. Christopher Depcik, Bram van Leer, and Dennis Assanis. The numerical simulation of variable-property reacting-gas dynamics: New insights and validation. *Numerical Heat Transfer, Part A: Applications*, 47(1):27–56, 2004.
23. V.I. Terekhov and M.A. Pakhomov. The numerical modeling of the tube turbulent gas-drop flow with phase changes. *International Journal of Thermal Sciences*, 43(6):595–610, 2004.
24. C. Baumgarten. *Mixture Formation in Internal Combustion Engines*. Heat and Mass Transfer. Springer, 2006.
25. M. Koebel, M. Elsner, and G. Madia. Reaction Pathways in the Selective Catalytic Reduction Process with NO and NO_2 at Low Temperature. *Ind. Eng. Chem. Res.*, 40:52–59, 2001.
26. S. D. Yim, S. J. Kim, J. H. Baik, I. S. Nam, Y. S. Mok, Lee J. H., Cho B. K., and S. H. Oh. Decomposition of Urea into NH_3 for the SCR process. *Ind. Eng. Chem. Res.*, 43:4856–4863, 2004.
27. R.J. LeVeque. *Finite Volume Methods for Hyperbolic Problems*. Cambridge Texts in Applied Mathematics. Cambridge University Press, 2002.
28. J.H. Ferziger and M. Perić. *Computational Methods for Fluid Dynamics*. Springer, 2002.
29. C. Hirsch. *Numerical Computation of Internal and External Flows: The Fundamentals of Computational Fluid Dynamics*. Number v. 1 in Butterworth Heinemann. Elsevier Science, 2007.
30. H. K. Versteeg and W. Malalasekera. *An Introduction to Computational Fluid Dynamics: the Finite Volume Method*. Addison-Wesley, Longman, 1995.
31. V. Yakhot, S. A. Orszag, S. Thangam, T. B. Gatski, and C. G. Speziale. Development of turbulence models for shear flows by a double expansion technique. *Physics of Fluids A: Fluid Dynamics*, 4(7):1510–1520, 1992.
32. F. R. Menter. Two-equation eddy-viscosity turbulence models for engineering applications. *AIAA Journal*, 32(8):1598–1605, 1994.
33. S. Fischer, R. Bitto, T. Lauer, and C. et al. Krenn. Impact of the turbulence model and numerical approach on the prediction of the ammonia homogenization in an automotive scr system. *SAE Int. J. Engines*, 5(3):1443–1458, 2012.
34. G. Stiesch. *Modeling Engine Spray and Combustion Processes*. Springer, 2003.
35. M. Boileau, S. Pascaud, E. Riber, B. Cuenot, L.Y.M. Gicquel, T.J. Poinsot, and M. Cazalens. Investigation of two-fluid methods for large eddy simulation of spray combustion in gas turbines. *Flow, Turbulence and Combustion*, 80:291–321, 2008.
36. S Hoyas, J.M. Pastor, D. Khuong-Anh, J. M. Momp-Laborda, and F. Ravet. Evaluation of the eulerian-lagrangian spray atomisation (elsa) in spray simulations. *Int. J. Vehicle Systems Modelling And Testing.*, 6(3/4), 2011.
37. F. V. Bracco. Modeling of Engine Sprays. *SAE Paper*, 850394, 1985.
38. R. D. Reitz. Modeling Atomization Processes In High Pressure Vaporizing Sprays. *Atomization and Spray Technology*, Vol. 3:pp. 309–337, 1987.
39. Henrik Str*a*m, Andreas Lundstr*a*m, and Bengt Andersson. Choice of urea-spray models in cfd simulations of urea-scr systems. *Chemical Engineering Journal*, 150(1):69–82, 2009.
40. G. D'Errico, D. Ettorre, and T. Lucchini. Simplified and Detailed Chemistry Modeling of Constant-Volume Diesel Combustion Experiments. *SAE Paper*, 2008-01-0954, 2008.
41. D. Stanton, A. Lippert, R. D. Reitz, and C. J. Rutland. Influence of Spray-Wall Interaction and Fuel Films on Cold Starting in Direct Injection Diesel Engines. *SAE Paper*, 982584, 1998.
42. A. V. Kolpakov et al. Calculation of the Rebound Condition for Colliding Drops of Sharply Different Sizes. *Kollodn. Zh.*, Vol. 47, 1985.
43. D.Stanton and C. J. Rutland. Modeling fuel film formation and wall interaction in diesel engines. *SAE Paper 960628*, 1996.
44. A. L. Yarin and D. A. Weiss. Impact of Drops on Solid Surfaces: Self-Similar Capillary Waves, and Splashing as a new Type of Kinematic Discontinuity. *Journal of Fluid Mechanics*, Vol. 283, 1995.
45. W. E. Ranz and W. R. Marshall. Evaporation from drops. *Chem. Eng. Prog.*, 48:141–146, 1952.

46. P. J. O'Rourke. Statistical Properties and Numerical Implementation of a Model for Droplet Dispersion in a Turbulent Gas. *Journal of Computational Physics*, Vol. 83:345–360, 1989.
47. R. J. Haywood, M. Renksizbulut, and G. D. Raithby. Numerical solution of deforming evaporating droplets at intermediate reynolds numbers. *Numerical Heat Transfer, Part A: Applications*, 26(3):253–272, 1994.
48. B.T Helenbrook and C.F Edwards. Quasi-steady deformation and drag of uncontaminated liquid drops. *International Journal of Multiphase Flow*, 28(10):1631–1657, 2002.
49. S. Kontin, A. Höfler, R. Koch, and H.-J. Bauer. Heat and mass transfer accompanied by crystallisation of single particles containing urea-water-solution. In *ILASS-Europe 2010 23rd Annual Conference on Liquid Atomization and Spray Systems*, Brno, Czech republic, September 2012.
50. A Lundström, B Waldheim, H Ström, and B Westerberg. Modelling of urea gas phase thermolysis and theoretical details on urea evaporation. *Proceedings of the Institution of Mechanical Engineers, Part D: Journal of Automobile Engineering*, 225(10):1392–1398, 2011.
51. Felix Birkhold, Ulrich Meingast, Peter Wassermann, and Olaf Deutschmann. Modeling and simulation of the injection of urea-water-solution for automotive scr denox-systems. *Applied Catalysis B: Environmental*, 70(14):119–127, 2007. Papers presented at the 4th International Conference on Environmental Catalysis (4th ICEC)Heidelberg, Germany, June 05 08, 2005.
52. J. W. Kiedaisch and S. P. Gravante. Calibration of cfd spray model parameters using detailed experimental sray characterization data. In *ICLASS 2009, 11th Triennial International Conference on Liquid Atomization and Spray Systems*, Vail, Colorado, US, July 2009.
53. D.T. Ryddner and M.F. Trujillo. A fully resolved uws droplet simulation. In *ILASS-Americas, 24th Annual Conference on Liquid Atomization and Spray Systems*, San Antonio, Texas, US, May 2012.
54. Tae Joong Wang, Seung Wook Baek, Seung Yeol Lee, Dae Hwan Kang, and Gwon Koo Yeo. Experimental investigation on evaporation of urea-water-solution droplet for scr applications. *AIChE Journal*, 55(12):3267–3276, 2009.
55. A Lundstrm, B Waldheim, H Strm, and B Westerberg. Modelling of urea gas phase thermolysis and theoretical details on urea evaporation. *Proceedings of the Institution of Mechanical Engineers, Part D: Journal of Automobile Engineering*, 225(10):1392–1398, 2011.
56. Andreas M. Bernhard, Izabela Czekaj, Martin Elsener, Alexander Wokaun, and Oliver Kröcher. Evaporation of urea at atmospheric pressure. *The Journal of Physical Chemistry A*, 115(12):2581–2589, 2011.
57. A. A. Kozyro, A. P. Krasulin, V. V. Simirskii, and V. S. Markovnik. Thermodynamic properties of tetramethylurea. *Russ. J. Phys. Chem. (Engl. Transl.)*, 62(10):895–897, 1988.
58. H. Foucart, C. Habchi, J. F. Le Coz, and T. Baritaud. Development of a three-dimensional model of wall fuel liquid film for internal combustion engines. *SAE Paper 980133*, 1998.
59. M. Trujillo and C. F. Lee. Modeling film dynamics in spray impingement. *Journal of Fluids Engineering*, 2003.
60. Ž. Tukovic and H Jasak. Simulation of free-rising bubble with soluble surfactant using moving mesh finite volume/area method. In *6th International Conference on CFD in Oil & Gas, Metallurgical and Process Industries*. SINTEF/NTNU, June 2008.
61. F. Birkhold, U. Meingast, P. Wassermann, and O. Deutschmann. Analysis of the injection of urea-water-solution for automotive scr denox-systems: Modeling of two-phase flow and spray/wall-interaction. *SAE Technical Papers*, 2006. cited By (since 1996)24.
62. H.G. Weller, G. Tabor, H. Jasak, and C. Fureby. A tensorial approach to computational continuum mechanics using object-oriented techniques. *Computers in Physics*, 12(6):620, 1998.
63. G. Montenegro, A. Onorati, F. Piscaglia, and G. D'Errico. Integrated 1D-MultiD Fluid Dynamic Models for the Simulation of I.C.E. Intake and Exhaust Systems. *SAE Technical Paper*, 2007-01-0495, 2007.

64. W.H. Press. *Numerical Recipes: The Art of Scientific Computing*. Cambridge University Press, 2007.
65. J. F. Le Coz, C. Catalano, and T. Baritaud. Application of laser induced fluorescence for measuring the thickness of liquid films on trasparent walls. In *7th Int. Symposium on application of laser techniques to fluid mechanics*, 1997.
66. T. Lucchini, G. D'Errico, G. M. Brusiani, F. and. Bianchi, Z. Tukovic, and H. Jasak. Multi-dimensional modeling of the air/fuel mixture formation process in a pfi engine for motorcycle applications. *SAE Technical Paper,*, 2009-24-0015, 2009.
67. H. Weltens, H. Bressler, F. Terres, H. Neumaier, H. Neumaier, and D. Rammoser. Optimisation of catalytic converter gas flow distribution by cfd prediction. *SAE Technical Paper*, 930780, 1993.
68. Thomas L. McKinley, Andrew G. Alleyne, and Chia-Fon Lee. Mixture non-uniformity in scr systems: Modeling and uniformity index requirements for steady-state and transient operation. *SAE International Journal of Fuels and Lubricants*, 3(1):486–499, 2010.